Model for the curvature response of the CDF II drift chamber

Ashutosh Vijay Kotwal *
Department of Physics, Duke University, Durham, North Carolina 27708, USA

(Received 25 July 2024; accepted 25 December 2024; published 3 February 2025)

The CDF II experiment at the Fermilab Tevatron used a drift chamber to measure the momenta of charged particles. We present a model for the response of the drift chamber to the curvature of a charged particle's trajectory. Constraints on the model parameters are obtained from cosmic-ray data and from information published by CDF in the context of the W boson mass measurement. Implications for the calibration of the drift chamber measurement of momentum are discussed. The robustness of the CDF calibration procedure is demonstrated. The model provides a framework for the analysis of precision magnetic trackers of high-momentum particles.

DOI: 10.1103/PhysRevResearch.7.013128

I. INTRODUCTION

The CDF II collider detector operated at the Fermilab Tevatron during 1999–2011. The central drift chamber of the CDF II experiment, called the central outer tracker (COT), measured the positions of charged particles as they traverse the active volume [1]. The cylindrical chamber was coaxial with the colliding beams and and was immersed in a 1.4 T axial magnetic field that bent charged particles in the plane transverse to the mutual axis. The particle positions were recorded by up to 96 wires sequentially in the outward radial direction. Half of the sense wires were axial and the remaining wires had a small stereo angle to collectively determine the particles' positions and directions in three dimensions. A helical fit is performed to the measured coordinates as a function of radius to infer the track parameters.

In the context of precision measurements like that of the W boson mass m_W, the CDF drift chamber is the crucial device because it provides the most important input—the measurement of the momenta of the muons and electrons that originate from the decay of W and Z bosons and the J/ψ and Υ mesons. The silicon vertex detector is not used in the CDF measurements of m_W because the improvement in the momentum resolution is marginal and there is no benefit to the analysis [2,3].

The helical trajectory of the particle in the axial magnetic field projects to a two-dimensional circle in the traverse plane. The circle's radius R is proportional to p_T, the momentum component transverse to the beam axis, and its curvature c is proportional to qR^{-1}, where $q = \pm 1$ is the particle's electric charge.[1] Therefore, in the natural units[2] of p_T^{-1} (typically GeV^{-1}), the curvature of the fitted track, $c^{\mathrm{measured}} \equiv (q/p_T)^{\mathrm{measured}}$ is a function of the true curvature $c \equiv q/p_T$. This is the most important response function since it is associated with the momentum calibration of the device.

We begin this discussion with the ansatz that an open-cell drift chamber in which the entire volume is active, instrumented and fiducial must have an analytic response function for high-p_T particles. In this context, analyticity refers to smoothness, i.e., continuity and differentiability. Later we expand the discussion to the implications of and constraints on nonanalytic behavior.

A salient feature of this drift chamber is that many of the terms in the general ansatz for the response function can be related to the fundamentals of the chamber's construction and operation. This feature enables the calibration of the device largely from first principles. Pushing this approach as far as possible maximizes the understanding of "how and why it works" in the sense of reductionism and critical rationalism [4] and avoids the black-box nature of very high-dimensional fitting or machine learning [5].

Guided by this philosophy, the goal of this paper is to analyze the drift chamber's calibration for the transverse momentum of charged particles. While the measurement of the polar angle is also important for the reconstruction of invariant masses from the 3-momenta of the daughter particles, the focus on the transverse momentum is motivated. Known effects such as sense-wire misalignment and particle energy loss induce a significant p_T-dependence to the momentum calibration, whereas the polar-angle measurement is much less sensitive to p_T-dependent effects. Hence, it is interesting to investigate the relationship between c^{measured} and c in the p_T-regime relevant to precision observables like m_W. In particular, we are interested in the deviations of this relationship from exact equality.

Since the invention of the multiwire proportional chamber [6], this device and its derivative, the drift chamber, have been used in a myriad of experiments in particle physics and more broadly in medicine, biology and radiation detection. Their capabilities in terms of precision, accuracy, particle rate and radiation tolerance have steadily increased. In conjunction

*Contact author: ashutosh.kotwal@duke.edu

[1]Experimentally, the particle's charge is determined from the sign of c^{measured}.

[2]We use natural units by setting the speed of light to unity.

with a magnet, these tracking devices have been used to measure particle momenta with high precision and accuracy, such as muons at 470 GeV by the E665 experiment [7,8]. Most recently, the CDF Collaboraton has published an m_W measurement using the COT-based magnetic tracker whose particle-momentum measurement has been calibrated to 25 parts per million (ppm) [2]. These and future precision momentum measurements with magnetic trackers motivate the analysis of these devices from first principles. This paper presents a framework for understanding the COT momentum calibration, that may also be applicable to the precision magnetic trackers of the experiments at the LHC [9–11], future colliders [12–16], and fixed-target experiments [17–19].

A. Analytic curvature response function

With no loss of generality, an analytic response function with spatial degrees of freedom can be written as a Taylor expansion around $c = 0$, the natural value of curvature in the absence of a magnetic field,

$$c^{\text{measured}} = a_0 + (1 + a_1 + b_1 q)c + (a_2 + b_2 q)c^2 + (a_3 + b_3 q)c^3 + ...,$$

where quartic and higher-order terms are not shown. It will be shown that, in the relevant range of p_T, uncertainties due the higher-order terms are encapsulated in the constraints on the parameters up to the cubic coefficients. This justifies the truncation of the Maclaurin expansion by information criteria [20].

The correspondence between the nomenclature used in this document and in previous CDF publications is described in Appendix A.

The $c \to 0$ limit corresponds to the straight-line trajectory of a charged particle with very high p_T when traversing an axial magnetic field. From the perspective of a tracking device, $c = 0$ is just as natural as the situation with zero magnetic field, when all charged-particle trajectories are straight lines. For this reason, the Maclaurin expansion above can equally well be considered as an expansion in the axial (z) component of the magnetic field (B), for a charged particle with a given p_T. In other words, the Maclaurin expansion can be re-interpreted as an expansion in B_z. In a thought experiment, one can dial B_z from negative to positive values and the curvature of the particle's trajectory (of fixed p_T) will respond proportionately to B_z. Since B_z can be varied continuously and smoothly, the curvature and its measurement must track this smooth variation.

A perfect spatial response, $c^{\text{measured}} = c$, implies that all a and b coefficients are zero. Therefore,

$$\delta c \equiv c^{\text{measured}} - c = a_0 + (a_1 + b_1 q)c + (a_2 + b_2 q)c^2 + (a_3 + b_3 q)c^3 + ...,$$

where c is defined at the beam axis. The latter coincides with the cylindrical axis of the COT, because the COT has been aligned with the beam axis for all running conditions using tracks of particles promptly produced in beam-beam collisions [2,21]. The procedure for matching the COT axis and the beam axis is described in Appendix B 1. The alignment between the COT and solenoid axes is discussed in Appendix B 2.

1. Charge dependence

The presence of the two types of coefficients in the Maclaurin expansion allows for separate charge-independent and charge-dependent imperfections that depend on the spatial (but not temporal) trajectory of the particle. This ansatz generalizes the model presented in Ref. [3].

The a_0 term represents the false curvature for a straight-line trajectory which is typically induced by misalignment of the tracker sensors. The a_1 coefficient represents the deviation from unity of the proportional momentum calibration factor, often referred to as the momentum scale factor or simply the momentum scale, and may be caused by the use of the incorrect value of the magnetic field or the tracker radius. The b_2 coefficient is mimicked by the ionization energy loss incurred upstream of the tracker. These terms represent charge-symmetric effects.

The drift cells are tilted to compensate for the Lorentz angle of the drifting electrons. The b_1, a_2, and b_3 coefficients capture effects that might break the charge symmetry due to this tilt. These charge-antisymmetric coefficients are shown to be negligible or have no impact on the CDF m_W measurement [2].

2. Energy loss

The energy ϵ lost by the charged particle as it traverses the tracker correlates with the temporal history of the particle. By convention, $\epsilon > 0$ when the particle traverses the tracker in the outward radial direction, i.e., a particle produced in a beam-beam collision or an outward-going cosmic ray (Fig. 1). For these particles, $p_T^{\text{measured}} = (p_T - \epsilon)$ since the COT measurement occurs after the particle (produced with p_T) traverses the beam pipe and the silicon detector which are situated upstream of the COT. The energy loss almost entirely occurs in these upstream devices and support structures. As a correction to p_T, ϵ is defined at normal incidence.

Figure 1 also shows that for an incoming cosmic ray, $p_T^{\text{measured}} = (p_T + \epsilon)$ since the COT measurement occurs before the particle loses energy in the material between the COT and the beam axis (where p_T is defined). To account for the bi-directional nature of cosmic-ray tracks, we introduce a binary variable t, with $t \equiv +1(-1)$ for an outgoing (incoming) cosmic-ray track; $t = +1$ for particles produced in beam-beam collisions (Fig. 1).

In Appendix C it is shown that the energy loss induces, up to third order, the corrections terms $(tq\epsilon c^2 + \epsilon^2 c^3)$ to the equation above,

$$\delta c = a_0 + (a_1 + b_1 q)c + (a_2 + [b_2 + t\epsilon]q)c^2 + ([a_3 + \epsilon^2] + b_3 q)c^3 + ... \quad (1)$$

Thus, the energy loss induces a b_2-like coefficient which is distinguishable from the spatial (geometry-induced) b_2 coefficient by comparing incoming ($t \equiv -1$) and outgoing ($t \equiv +1$) cosmic-ray tracks. The energy loss also induces an a_3-like coefficient at second order which is indistinguishable from geometrical sources of a_3.

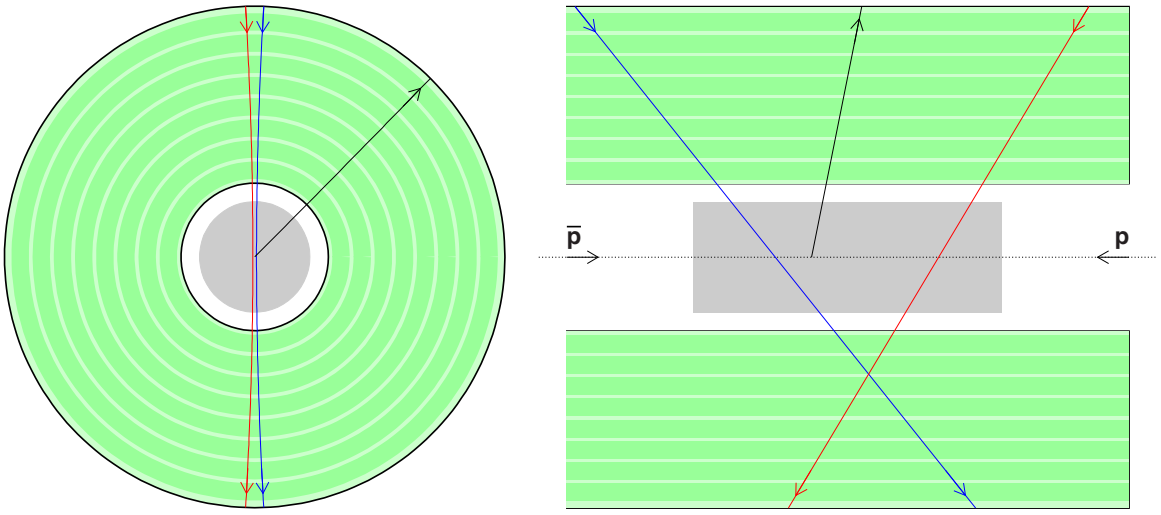

FIG. 1. Schematics of the CDF II experiment's cylindrical drift chamber (COT) in the transverse (azimuthal) view (left) and longitudinal view (right). The beam line is along the longitudinal axis of the tracker, which is also the direction of the magnetic field. The green-shaded region shows the active gas-filled volume, between radii of 40 and 138 cm from the cylinder (and beam) axis [1]. The eight darker-green annuli depict the superlayers (rings of supercells) as shown in Fig. 4. The gray shading indicates the region occupied by the silicon tracking detector. The red and blue trajectories illustrate two oppositely charged cosmic-ray muons propagating downward in azimuth, each of $p_T = 10$ GeV. Their impact parameter of ± 1 cm is typical of the cosmic-ray sample analyzed in this paper and in Ref. [21]. Also shown as the black trajectory is a muon with $p_T = 40$ GeV emanating from a decaying W boson. The arrows indicate the direction of propagation. The complete cosmic-ray trajectory is referred to as the dicosmic because it is comprised of the incoming (pointing towards the beam axis) and outgoing (pointing away from the beam axis) legs of the cosmic-ray path.

Hard scattering from the drift chamber wires is a negligible effect, as discussed in Appendix C.

3. Spatial uniformity

The coefficients a_n, b_n, and ϵ of the response function may initially depend on the azimuthal and polar angle at which the particle traverses the drift chamber. Averaged over c, these dependencies have been eliminated by an alignment procedure[3] that makes the COT response uniform with respect to orientation [21]. A summary of the spatial uniformity of the COT is provided in Appendix D.

We will show that by far the largest sources of systematic uncertainty in the momentum calibration of the COT are the a_1 and ϵ parameters.

The curvature proportionality parameter a_1 depends on the COT radius and the magnetic field. The COT radius is defined by its end plates and cannot depend on polar angle. The wires deviate from a straight-line shape due to gravitational and electrotatic deflections. A detailed analysis and corrections for these deflections are presented in Ref. [21] and summarized in Appendix D. A more significant source of polar-angle dependence of a_1 is the nonuniformity of the magnetic field due to the fringe-field effect at the edges of the solenoid. This effect is measured and corrected for using the $J/\psi \to \mu\mu$ data [2,3,24].

The energy loss ϵ is proportional to the length of the path traversed; for the high-p_T particles used in the m_W analysis [2], the dependence of the path length on the curvature is negligible and the latter scales solely as $(\csc\theta)$ where θ is the polar angle in cylindrical coordinates. As ϵ is defined at normal incidence, its impact on the measured curvature is nearly independent of θ. While the distribution of material along the beam axis is not perfectly uniform due to the placement of silicon-detector bulkheads, the dependence of ϵ on this cylindrical z coordinate is averaged over in a sufficiently similar way by all data samples used in the m_W analysis. The tracking detectors are also fairly symmetric in azimuth [1,22].

Thus, the salient features of the COT response are captured by an inclusive study of the a_n, b_n, and ϵ coefficients. A quantitative assessment of this conclusion is provided in Appendix D.

B. Nonanalytic response

It is conceivable that gaps in the acceptance of a tracking detector due to uninstrumented or dead regions, or boundaries between sensors lead to nonanalytic behavior of the response function. An investigation of this possibility is presented in Sec. VI in the form of $(a_r + b_r q)|c|^r$ terms with negative or fractional values of r. We find that the worst-case scenario is adequately parameterized by a $b_0 q$ term; other terms are either redundant or inconsistent with the COT being a single, unfragmented tracking volume. Thus, Eq. (1) may be fully generalized by including this term. In Sec. VI we discuss constraints on b_0 from studies of COT hit efficiency and drift displacement in the $c \to 0^{\pm}$ limit.

II. CONSTRAINTS FROM COSMIC-RAY TRACKS

Cosmic rays provide a powerful control sample of data that CDF has used to pin down many attributes of the drift

[3]This average was performed such that $\langle c \rangle \equiv 0$ for the alignment-data sample [21].

chamber. There are two salient features of this sample. First, high-p_T cosmic-ray muons are automatically selected by the same trigger paths that acquire the W and Z boson data in the muon channel. This feature guarantees that the cosmic-ray events are chosen in situ with collider data and that they experience the same operating conditions of the detector as the collider data used for physics analysis. The trigger-timing requirements ensure that these cosmic rays are synchronous with proton-antiproton collisions within a few nanoseconds [23]. In addition to the five spatial parameters that characterize tracks originating from $p\bar{p}$ collisions, cosmic-ray tracks include the beamline-crossing time and the direction of propagation as fitted parameters. These track-fitting procedures ensure the equivalence of the fitted spatial parameters between the two types of tracks [23]. For these reasons, measurements of the drift chamber made with cosmic rays are usable for reconstructed tracks in collider data.

Second, cosmic rays traversing the COT through all its radial layers, and passing close to the beam axis, contain a very useful redundancy that CDF exploits for accurate calibration. Figure 1 shows that cosmic rays provide an excellent data sample for tracker alignment and bias measurement [21]. The comparison of the two legs of the reconstructed cosmic-ray trajectory provides an estimate of track parameter biases because the two legs provide independent measurements of the same particle (up to the muon's ionization energy loss as it traverses the silicon tracker) [21]. The distribution of the cosmic rays is fairly uniform in azimuth and in polar angle.

The measured curvature of the outgoing leg is

$$c^{\text{out}} = a_0 + (1 + a_1 + b_1 q)c + (a_2 + [b_2 + \epsilon]q)c^2 + (a_3 + \epsilon^2 + b_3 q)c^3 + ...,$$

and the incoming leg is reconstructed as a muon of the opposite charge, $c \to -c$ and $q \to -q$, which is also time-reversed, $t \to -t$,

$$\begin{aligned} c^{\text{in}} &= a_0 + (1 + a_1 - b_1 q)(-c) + (a_2 - [b_2 - \epsilon]q)(-c)^2 \\ &\quad + (a_3 + \epsilon^2 - b_3 q)(-c)^3 + ... \\ &= a_0 + (-1 - a_1 + b_1 q)c + (a_2 - b_2 q + \epsilon q)c^2 \\ &\quad + (-a_3 - \epsilon^2 + b_3 q)c^3 + ... \end{aligned}$$

Therefore,

$$\Delta_c^+ = \tfrac{1}{2}(c^{\text{out}} + c^{\text{in}}) = a_0 + b_1 qc + (a_2 + \epsilon q)c^2 + b_3 qc^3 + ... \quad (2)$$

and

$$\Delta_c^- = \tfrac{1}{2}(c^{\text{out}} - c^{\text{in}}) = (1 + a_1)c + b_2 qc^2 + (a_3 + \epsilon^2)c^3 + ... \quad (3)$$

For the right-hand side of these equations, the true value of c is well-represented by the measurement of the "dicosmic helix," which is described in Refs. [21,23]. The dicosmic helix fit is performed on the combined set of COT hits associated with the incoming and outgoing legs together (Fig. 1). The direction of the momentum of the cosmic-ray muon is taken into account in this fit (and in the separate fits to the incoming and outgoing legs for the measurement of c^{in} and c^{out}, respectively) by adjusting each drift chamber hit coordinate for the appropriate time-of-flight delay [23]. The same time-of-flight delay is included in the helix fit to all outgoing drift-chamber tracks of particles emanating from beam-beam collisions that are used for physics analysis.

The curvature measurement c_{d} from the dicosmic helix fit is more precise than the measurements of c^{in} and c^{out} by a factor of $8\sqrt{2}$, due to the track length increase from 96 cm to 274 cm and the doubling of the number of hits. Hence, the dicosmic helix measurement provides a good proxy for the true c. The corollary is that $\text{sgn}(c_{\text{d}})$ is a good proxy for q as long as we avoid sensitivity to resolution-induced bias. The resolution of c^{in} and c^{out} is measured to be 1.3 TeV^{-1} [21], therefore the resolution of c_{d} is expected to be 110 PeV^{-1}.

The cosmic-ray data presented here are identical to the data presented in Ref. [21]. The track impact parameter (d_0) with respect to the beam axis is distributed such that $|d_0| < 3$ cm and the z coordinate of the tracks' point of closest approach to the beam axis (z_0) is required to be within 60 cm of the beam-beam collision point. These conditions ensure that the cosmic-ray tracks have similar trajectories as the particles selected for the m_W measurement [2].

A. Constraints from Δ_c^+

The measurement of Δ_c^+ as a function of c_{d} is shown in Fig. 2. The five-parameter fit of Eq. (2) to the data is superposed, along with the fitted values of the parameters. Since these data are post-alignment [21], it is expected that the fitted value of a_0 is statistically consistent with zero. The remaining parameters provide new information about the COT response. As shown in Appendix E 1, this analysis is expected to provide accurate measurements of the coefficients in Eq. (2).

The fit to these cosmic-ray data finds a value for the energy loss $\epsilon = (9.71 \pm 0.65_{\text{stat}})$ MeV. This measurement is consistent with the value[4] quoted in Sec. V B3 of Ref. [3], "Each muon passing through the silicon and COT detectors loses on average 9 MeV at normal incidence." As the ϵ term is the only term odd in q in Eq. (2), ϵ is minimally correlated with the other parameters; the largest correlation coefficient between ϵ and any other parameter is 8%.

Since the alignment procedure [21] brings a_0 close to zero, it is a redundant parameter in the fit shown in Fig. 2 (left). The fit is repeated after constraining $a_0 = 0$ to obtain the appropriate constraints on the parameters b_1, a_2 and b_3. As shown in Fig. 2 (right), the latter are found to be statistically consistent with zero, implying the absence of these imperfections in the COT within the respective precisions. The uncertainties on these parameters will be used to bound the corresponding uncertainties in the m_W measurement in Sec. IV. In this fit, a_2 is strongly anticorrelated with b_1 and b_3, with correlation coefficients of -97% and -98%, respectively.

[4]The first-principles value of ϵ is obtained in Refs. [2,3] by *ab initio* calculation of the energy loss, based on published formulas and a fine-grained three-dimensional lookup table of the amount of ionizing material used during construction of the silicon tracker and the COT.

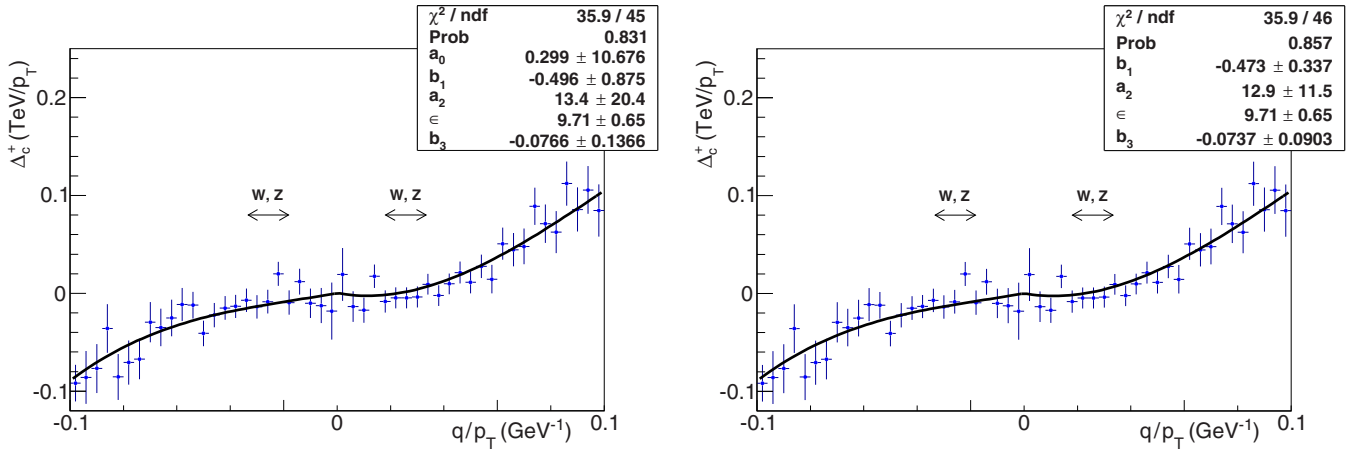

FIG. 2. The measurement of Δ_c^+ as a function of $c_{\rm d}$, the measured curvature of the COT dicosmic helix, in cosmic-ray data collected in situ during collider operation. The requirement $|z_0| < 60$ cm ensures that the cosmic-ray tracks have similar trajectories as the particles selected for physics analysis. Also shown are the fits to Eq. (2) and the values and statistical uncertainties of the fitted parameters (left) a_0 (in PeV^{-1}), b_1 (in ‰), a_2 and ϵ (both in MeV), and b_3 (in GeV^2), and (right) b_1, a_2 and ϵ, and b_3. The error bars indicate the statistical uncertainties on the data points. The horizontal arrows indicate the range of q/p_T of the leptons originating from $W^\pm \to \ell^\pm\nu$ and $Z \to \ell^+\ell^-$ decays that are used in the m_W analysis [2].

B. Comment on Δ_c^-

The measurement of Δ_c^- as a function of c, if the true c were known, would provide information on the coefficients in Eq. (3). However, if $c_{\rm d}$ is used as a proxy for c, then no information can be extracted from Δ_c^-, as shown in Appendix E 2.

III. CONSTRAINT FROM POSITRON-ELECTRON DIFFERENCE OF $\langle E/p\rangle$

The calorimeter measurement of the energy E of electrons and positrons is combined with the polar-angle measurement of the track to obtain their transverse energy E_T. For electrons and positrons of the same momentum incident at the same location of the calorimeter, their electromagnetic shower energies are identical within $(1\,\text{MeV})/E \sim (1\,\text{MeV})/(40\,\text{GeV}) \lesssim 30$ ppm, where 40 GeV is the relevant E_T for W and Z boson decays and 1 MeV is the additional energy released from the positron annihilation. Hence, the difference of $\langle E_T/p_T\rangle$ between positrons and electrons is used to constrain the tracker bias in the measurement of p_T.

Using the calibrated measurement of E_T as a proxy for q/c, we write this difference as

$$\begin{aligned}
\Delta_{pe} &\equiv \frac{1}{2}\left[\left\langle\frac{E_T}{p_T}(e^+)\right\rangle - \left\langle\frac{E_T}{p_T}(e^-)\right\rangle\right] = \frac{1}{2}\Sigma_q q\left\langle\frac{E_T}{p_T}\right\rangle \\
&= \frac{1}{2}\Sigma_q \frac{q}{c}c^{\text{measured}} = \frac{1}{2}\Sigma_q\frac{q}{c}(c+\delta c) \\
&= \frac{1}{2}\Sigma_q q\frac{\delta c}{c} = \frac{1}{2}\Sigma_q\frac{q}{c}[a_0 + (a_1+b_1 q)c + (a_2+b_2' q)c^2 \\
&\quad + (a_3+\epsilon^2+b_3 q)c^3] \\
&= \frac{1}{2}\Sigma_q\Big[a_0\frac{q}{c} + (a_1 q + b_1) + (a_2 q + b_2')c \\
&\quad + (a_3 q + \epsilon^2 q + b_3)c^2\Big] \\
&= a_0\langle p_T\rangle + b_1 + a_2\langle p_T^{-1}\rangle + b_3\langle p_T^{-2}\rangle \qquad (4)
\end{aligned}$$

since $a_1\Sigma_q q$, $b_2'\Sigma_q c$ and $\Sigma_q(a_3+\epsilon^2)qc^2$ vanish by charge symmetry. The combination of the two coefficients $b_2' \equiv b_2 + \epsilon$ is motivated in Sec. IV A.

In the m_W analysis [2], tracks are calibrated to eliminate this difference so that $\Delta_{pe} = 0 \pm 43$ ppm. The statistical uncertainty on Δ_{pe} is the same[5] as the statistical uncertainty on the fit to the inclusive E_T/p_T distribution shown in Ref. [2]. The bias on Δ_{pe} due to the positron annihilation energy of $\lesssim 15$ ppm is negligible compared to the statistical uncertainty.

As this method calibrates a quantity linear in δc, there is no need to consider higher powers of δc.

A. Bremsstrahlung

While muons experience ionization energy loss as they traverse the inner silicon vertex detector, electrons/positrons also undergo energy loss due to bremsstrahlung photon radiation. The radiated photons are almost always coalesced with the calorimeter shower produced by the primary $e^\pm$. In these radiative cases, E_T (p_T) measures the primary $e^\pm$ before (after) the bremsstrahlung emission and the spectrum of E_T/p_T has a high-side radiative tail (e.g., Fig. 2(B) of Ref. [2]). Nonradiative $e^\pm$ candidates are selected for the Δ_{pe} measurement by requiring $0.9 < E_T/p_T < 1.1$ [2,24]. The interval isolates the resolution-broadened peak of E_T/p_T near unity. The soft bremsstrahlung within this interval acts as a percent-level scale factor on Δ_{pe} which is irrelevant when the alignment brings Δ_{pe} to zero.

IV. BIAS IN INVARIANT-MASS FITS

The reconstruction of the invariant mass m of a neutral particle from its two-body decay into massless particles can

[5]Taking the difference between two half-samples increases the statistical uncertainty by a factor of $\sqrt{2}\times\sqrt{2}$ which is canceled by the factor of $\frac{1}{2}$ in the definition of Δ_{pe}.

be written as follows:

$$m^2 = (p_1 + p_2)^2 = 2p_1.p_2 = 2E_1E_2(1 - \cos\gamma)$$
$$= 2p_{T1}p_{T2}(1 - \cos\gamma)/(\sin\theta_1 \sin\theta_2),$$

where γ is the opening angle between the 3-vectors of the daughters and $\theta_{1,2}$ are their respective polar angles. Since the uncertainty on the angle measurements has a negligible contribution to the mass uncertainty in comparison to the curvature uncertainty,[6]

$$m^2 \propto 2p_{T1}p_{T2} = 2\frac{q_1}{c_1}\frac{q_2}{c_2} = \frac{-2}{c_1c_2}.$$

A. First-order effects on mass reconstruction

The bias in the measured mass, δm caused by the COT biases is

$$m\delta m|_{1\text{st}} \propto \frac{1}{c_2}\frac{\delta c_1}{c_1^2} + \frac{1}{c_1}\frac{\delta c_2}{c_2^2}$$

at first order and the corresponding fractional mass bias is

$$\left.\frac{\delta m}{m}\right|_{1\text{st}} = \left(\frac{1}{c_2}\frac{\delta c_1}{c_1^2} + \frac{1}{c_1}\frac{\delta c_2}{c_2^2}\right)/m^2 = \left(\frac{1}{c_2}\frac{\delta c_1}{c_1^2} + \frac{1}{c_1}\frac{\delta c_2}{c_2^2}\right)\frac{c_1c_2}{-2}$$
$$= \frac{-1}{2}\left(\frac{\delta c_1}{c_1} + \frac{\delta c_2}{c_2}\right).$$

Using the response model of Eq. (1), the fractional mass bias can be expressed in terms of the a, b, and ϵ coefficients. The first bias term is $-a_0\langle c^{-1}\rangle = -a_0\langle q \cdot p_T\rangle$ which averages to zero since the decay is charge-symmetric. Therefore, a_0 can only induce a mass bias at quadratic order, and by dimensional analysis the fractional mass bias must be proportional to $(a_0p_T)^2$, as shown in Sec. IV B.

The next terms causing a fractional mass bias are $\frac{1}{2}\Sigma_q(a_1 + b_1q)$. The b_1 term cancels between the two opposite charges and is not observable in the invariant mass. The a_1 term is the momentum calibration correction and therefore the fractional mass bias is proportional to a_1. Thus, $a_1 = 0$ after the precise calibration based on the $J/\psi \to \mu\mu$ and $\Upsilon \to \mu\mu$ mass fits and the corresponding uncertainty has been incorporated in the m_W analysis [2].

The next two terms causing a mass bias are $\frac{1}{2}\Sigma_q(a_2 + [b_2 + t\epsilon]q)c$. Again by the charge symmetry of the decay, $a_2\Sigma_q c = 0$ so a_2 is not visible in an inclusive mass fit.[7]

As invariant mass fits are performed for outgoing particles only (emanating from beam-beam collisions), $t = 1$ in this context (see Sec. I) and we can use the combined $b_2 + \epsilon = b_2'$ for this discussion. The term $\frac{1}{2}b_2'\Sigma_q qc = \frac{1}{2}b_2'\Sigma_q p_T^{-1} = b_2'\langle p_T^{-1}\rangle$. Thus, the slope of $\delta m/m$ versus $\langle p_T^{-1}\rangle$ measures b_2'. The b_2' coefficient is tuned from the $J/\psi \to \mu\mu$ mass fits in bins of $\langle p_T^{-1}\rangle$ with an uncertainty of 34 keV in the m_W analysis [2]. Thus, we can set $b_2' = 0$ after this calibration. The corresponding uncertainty at the three mass scales is

(1) at m_W and m_Z, $p_T \sim 40$ GeV: (34 keV)/(40 GeV) ~1 ppm,

(2) at m_Υ, $p_T \sim 5$ GeV: (34 keV)/(5 GeV) ~7 ppm,

(3) at $m_{J/\psi}$, $p_T \sim 3.3$ GeV: (34 keV)/(3.3 GeV) ~10 ppm.

This uncertainty on $m_{W,Z}$ is negligible and the uncertainty on m_Υ and $m_{J/\psi}$ is included in the m_W analysis [2].

The next two terms causing a mass bias are $\Sigma_q([a_3 + \epsilon^2] + b_3q)c^2$. Again by the charge symmetry of the decay, $b_3\Sigma_q qc^2 = 0$ so b_3 is not visible in an inclusive mass fit. Therefore, the surviving term is $[a_3 + \epsilon^2]\langle c^2\rangle$. The order of magnitude of the ϵ^2 term at the three relevant mass scales is

(1) at m_W and m_Z, $p_T \sim 40$ GeV: $\epsilon^2\langle c^2\rangle \sim [(9\,\text{MeV})/(40\,\text{GeV})]^2 \sim 0.1$ ppm,

(2) at m_Υ, $p_T \sim 5$ GeV: $\epsilon^2\langle c^2\rangle \sim [(9\,\text{MeV})/(5\,\text{GeV})]^2 \sim 3$ ppm,

(3) at $m_{J/\psi}$, $p_T \sim 3.3$ GeV: $\epsilon^2\langle c^2\rangle \sim [(9\,\text{MeV})/(3.3\,\text{GeV})]^2 \sim 7$ ppm.

Not only are these energy-loss effects small at quadratic order, they are already accounted for in the simulated lineshape templates used for these mass fits [2], with vanishing uncertainty.

In principle, the $J/\psi \to \mu\mu$ data can be used to measure a_3 by fitting for a quadratic dependence of $\delta m/m$ versus $\langle p_T^{-1}\rangle$. In practice, the linear fit to these data using a_1 and b_2' as free parameters is found to be consistent with the data within their uncertainties [2]. By the Akaike information criterion (AIC) [20], this implies that the inclusion of a_3 as a fit parameter would find a statistically insignificant value, and that the a_3 uncertainty is already accounted for when the uncertainties on a_1 and b_2' are propagated to low p_T^{-1}. This procedure is conservative because the effect of a_3 vanishes more rapidly as $p_T^{-1} \to 0$ than the effect of b_2'; therefore, absorbing the uncertainty due to a_3 into the uncertainty due to b_2' overestimates the propagated m_W uncertainty.

An independent upper bound on the uncertainty due to a_3 is obtained by comparing the $J/\psi \to \mu\mu$ and $\Upsilon \to \mu\mu$ data, as discussed below.

We conclude that a mass measurement is biased at first order by the parameters a_1, b_2' and a_3, while the remaining parameters a_0, b_1, a_2, and b_3 do not introduce a first-order bias. The uncertainties due to a_1, b_2', and a_3 are already accounted for in the m_W analysis [2].

B. Second-order effects on mass reconstruction

We evaluate the mass bias induced at second order by the curvature response function. Considering the second-order

[6]The uncertainty due to the polar angle is 4 ppm, 8 ppm, and 11 ppm, respectively, for the J/ψ, Υ, and Z boson mass measurement [2]. These uncertainties have minimal impact given the total uncertainties of 29 ppm, 36 ppm, and 70 ppm on the respective momentum calibrations derived from these data [2]. The azimuthal angle is measured 5 × (30×) more accurately than the polar angle [21] without (with) the beam constraint, and does not contribute an uncertainty on the mass measurements.

[7]The a_2 term should be visible as the slope in a plot of $\delta m/m$ versus $\langle c\rangle$.

derivatives,

$$m\delta m|_{\rm 2nd} \propto -2\frac{1}{c_2}\frac{(\delta c_1)^2}{c_1^3} - 2\frac{1}{c_1}\frac{(\delta c_2)^2}{c_2^3} - 2\frac{\delta c_1}{c_1^2}\frac{\delta c_2}{c_2^2},$$

$$\begin{aligned}\left.\frac{\delta m}{m}\right|_{\rm 2nd} &= c_1c_2\left(\frac{1}{c_2}\frac{(\delta c_1)^2}{c_1^3} + \frac{1}{c_1}\frac{(\delta c_2)^2}{c_2^3} + \frac{\delta c_1}{c_1^2}\frac{\delta c_2}{c_2^2}\right)\\ &= \left(\frac{\delta c_1}{c_1}\right)^2 + \left(\frac{\delta c_2}{c_2}\right)^2 + \frac{\delta c_1}{c_1}\frac{\delta c_2}{c_2}\\ &= \left(\frac{\delta c_1}{c_1} + \frac{\delta c_2}{c_2}\right)^2 - \frac{\delta c_1}{c_1}\frac{\delta c_2}{c_2}\\ &= \left(2\frac{\delta m}{m}|_{\rm 1st}\right)^2 - \Pi_q(A + qB),\end{aligned}$$

where

$$A \equiv a_1 + b_2'|c| + a_3c^2 = a_1 + b_2'/p_T + a_3/p_T^2 \qquad (5)$$

contains the terms of the response function that induce a first-order bias and

$$\begin{aligned}B &\equiv q(a_0/c + b_1q + a_2c + b_3qc^2)\\ &= a_0p_T + b_1 + a_2/p_T + b_3/p_T^2\end{aligned} \qquad (6)$$

contains the terms that do not induce a first-order bias. Note that A and B are symmetric in charge, and $\delta c/c \equiv A + qB$.

In Sec. IV A it was shown that the first-order fractional mass bias was equal to A. Thus, at second order,

$$\begin{aligned}\left.\frac{\delta m}{m}\right|_{\rm 2nd} &= (2A)^2 - (A+B)(A-B) = B^2 + 3A^2 \approx B^2\\ &= \Pi_q\left(a_0p_T + b_1 + a_2p_T^{-1} + b_3p_T^{-2}\right),\end{aligned}$$

where the product is over the two (oppositely charged) daughter particles. The square of the first-order bias $A^2 < (10^{-4})^2$ is negligible; therefore, the second-order fractional mass bias is approximated by B^2.

1. Second-order effects at the $m_{W,Z}$ scale

Figure 2 provides the following estimates of the uncertainties due to each of the terms in the second-order fractional mass bias, at a typical $p_T \sim 40$ GeV, using the expression for B^2:

(1) a_0 term: $(11\,\text{PeV}^{-1} \cdot 40\ \text{GeV})^2 \sim (440\ \text{ppm})^2 \sim 0.2$ ppm,
(2) b_1 term: $(0.5\,‰)^2 \sim 0.3$ ppm,
(3) a_2 term: $(\frac{14\,\text{MeV}}{40\,\text{GeV}})^2 \sim 0.2$ ppm,
(4) b_3 term: $[(0.09\,\text{GeV}^2)(40\,\text{GeV})^{-2}]^2 \sim (60\,\text{ppm})^2 \sim 3$ ppb (parts per billion).

These estimates show that, even ignoring the large anticorrelation between these coefficients as inferred from the fits in Fig. 2, the second-order bias in W and Z boson mass fits is expected to be negligible.

In the next two sections the effect of the large anticorrelation between these coefficients is estimated by removing redundant parameters in the fit to the cosmic-ray data (Fig. 2). We will find that the uncertainty on a_2 reduces by a factor of 5, thereby reducing its second-order effect at the $m_{W,Z}$ scale by a factor of 25 to 8 ppb. Thus, only a_0 and b_1 are relevant for estimating the second-order effects at the $m_{W,Z}$ scale. This is expected since a_0 and b_1 are low-curvature terms while a_2 and b_3 are high-curvature terms.

For the same reason, the observables obtained from the $W \to \ell\nu$ data, Δ_{pe} (see Sec. III) and $\Delta_W^{\mp}$ (to be introduced in Sec. V A) constrain a_0 and b_1 but not a_2 and b_3.

2. Second-order effects at the m_Υ scale

Since b_1 is dimensionless, the insignificant second-order bias induced by this parameter is independent of curvature and the mass being reconstructed. Hence, it is a negligible parameter and can be removed from the response model. Similarly, as the energy loss ϵ is measured precisely from the $J/\psi \to \mu\mu$ data and incorporated in the b_2' parameter, we can correct the cosmic-ray measurements for its known value (which is consistent with the fitted value in Fig. 2) and remove it as a free parameter.

The elimination of redundant parameters is equivalent to propagating the covariance matrix (including correlation coefficients that approach -1 for redundant parameters) on the original, complete set of parameters. In practice, redundant parameters lead to numerical instabilities; hence the removal of redundant parameters yields robust estimates.

With only a_2 and b_3 as free parameters, the fit to Δ_c^+ as a function of $c_{\rm d}$ provides more information on these parameters, as shown in Fig. 3. The χ^2/dof is improved relative to Fig. 2, confirming that a_0, b_1 and ϵ are redundant parameters per the AIC.

The second-order bias in the $\Upsilon \to \mu\mu$ mass fit, with a typical $p_T \sim 5$ GeV, is

(1) a_0 term: $(11\,\text{PeV}^{-1} \times 5\ \text{GeV})^2 \sim (55\ \text{ppm})^2 \sim 3$ ppb,
(2) b_1 term: $(0.5\,‰)^2 \sim 0.3$ ppm,
(3) a_2 term: $(\frac{3\,\text{MeV}}{5\,\text{GeV}})^2 \sim 0.4$ ppm,
(4) b_3 term: $[(0.036\,\text{GeV}^2)(5\,\text{GeV})^{-2}]^2 \sim (1.4\,‰)^2 \sim 2$ ppm.

Note that the correlation coefficient between the fitted values of a_2 and b_3 in Fig. 3 (left) is -97%, which means their combined bias is limited to 1.6 ppm. The uncertainties due to a_0, b_1 and a_2 are negligible compared to the total quoted uncertainty on the momentum calibration of 25 ppm [2], even without including their large anti-correlation, further justifying their elimination from the fit of Fig. 3.

Since the largest effect is due to b_3, the fit to Δ_c^+ as a function of $c_{\rm d}$ with only b_3 as the free parameter is shown in Fig. 3 (right). A small bias $b_3 = (0.023 \pm 0.008)\ \text{GeV}^2$ is discernible, corresponding to negligible bias of 1 ppm on the $\Upsilon \to \mu\mu$ mass fit.

3. Second-order effects at the $m_{J/\psi}$ scale

A similar analysis for the typical $p_T \sim 3.3$ GeV in the $J/\psi \to \mu\mu$ data sample shows the following second-order mass bias:

(1) a_0 term: $(11\,\text{PeV}^{-1} \times 3.3\ \text{GeV})^2 \sim (37\ \text{ppm})^2 \sim 1$ ppb,
(2) b_1 term: $(0.5\,‰)^2 \sim 0.3$ ppm,
(3) a_2 term: $(\frac{3\,\text{MeV}}{3.3\,\text{GeV}})^2 \sim 0.8$ ppm,

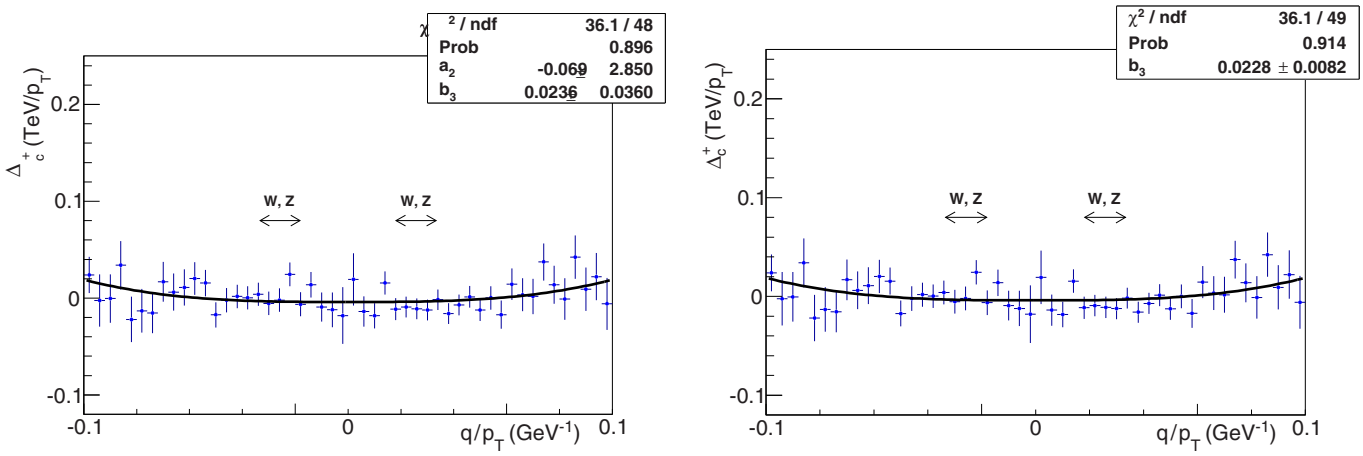

FIG. 3. The measurement of Δ_c^+ as a function of c_d, the measured curvature of the COT dicosmic helix, in cosmic-ray data collected in situ during collider operation. The requirement $|z_0| < 60$ cm ensures that the cosmic-ray tracks have similar trajectories as the particles selected for physics analysis. The data have been corrected for the known energy loss ϵ. Also shown are the fits to Eq. (2) and the values and statistical uncertainties of the fitted parameters (left) a_2 (in MeV), and b_3 (in GeV^2), and (right) b_3. The error bars indicate the statistical uncertainties on the data points. The horizontal arrows indicate the range of q/p_T of the leptons originating from $W^\pm \to \ell^\pm \nu$ and $Z \to \ell^+\ell^-$ decays that are used in the m_W analysis [2].

(4) b_3 term: $[(0.023\,\mathrm{GeV}^2)(3.3\,\mathrm{GeV})^{-2}]^2 \sim (2.1\,‰)^2 \sim$ 5 ppm.

Thus, the cosmic-ray data constrain the possible bias in the $J/\psi \to \mu\mu$ data due to the b_3 term to 5 ppm which is much smaller than the systematic uncertainty of 25 ppm quoted for the momentum calibration uncertainty from these data [2].

We conclude that the constraints on the "B" parameters of Eq. (6) from cosmic-ray data result in negligible uncertainty at all mass scales.

C. Additional bounds on a_3 and b_3 from J/ψ and Υ data

The cosmic-ray data have a curvature range $0 < |c|\,\mathrm{GeV} < 0.1$ which limits the precision on the b_3 parameter whose effects are only visible at high curvature. The $J/\psi \to \mu\mu$ and $\Upsilon \to \mu\mu$ data extend the curvature range to $0.2 < |c|\,\mathrm{GeV} < 0.45$ and provide additional bounds on the a_3 and b_3 parameters.

1. Bound on a_3

The comparison of the mass fits to the $\Upsilon \to \mu\mu$ and $J/\psi \to \mu\mu$ data yields the following information. The fractional bias on m_Υ ($m_{J/\psi}$) due to a_3 is $5^{-2}a_3$ ($3.3^{-2}a_3$). The difference between the momentum calibrations extracted from these data is 20 ppm, consistent with the uncertainty on this difference [2]. This implies that $a_3(3.3^{-2}$–$5^{-2}) \lesssim 20$ ppm, which bounds the uncertainty in extrapolating to m_W to $a_3(5^{-2}$–$40^{-2})$ to 15 ppm.

As the impact of a_3 grows with curvature, the range of $|c|$ spanned by the $J/\psi \to \mu\mu$ data yields additional information. The momentum calibration in the bins of largest $|c| \sim 0.43$ GeV^{-1} differs from the momentum calibration derived from the remainder of the bins (whose typical $|c| \sim 0.3$ GeV^{-1}) by 20 ppm [2]. This implies that $a_3(0.43^2$–$0.3^2) \lesssim 20$ ppm, which bounds the uncertainty in extrapolating to m_W to $a_3(0.3^2$–$40^{-2})$ to 19 ppm. Note that this small deviation observed in the largest $|c|$ bins is the source of the largest systematic uncertainty quoted in the momentum calibration from the $J/\psi \to \mu\mu$ data in the CDF m_W analysis [2].

These two constraints together bound any effect of a_3 to 12 ppm. From the data presented in Ref. [2] (Fig. 2), one notes that an attempt to extract a_3 from each of the above comparisons would yield two values of opposite sign. Thus, the combined value of a_3 would be much smaller than its estimated uncertainty of 12 ppm.

We conclude that, while the $J/\psi \to \mu\mu$ data and the $\Upsilon \to \mu\mu$ data together suggest a vanishing value of a_3, the rather tight bound on it is already included as an uncertainty on the momentum calibration in Ref. [2].

2. Bound on b_3

The comparison of the mass fits to the $\Upsilon \to \mu\mu$ and $J/\psi \to \mu\mu$ data can also yield information on b_3. The fractional bias on m_Υ ($m_{J/\psi}$) due to b_3 is $5^{-4}b_3^2$ ($3.3^{-4}b_3^2$). The consistency of these calibrations implies that $b_3^2(3.3^{-4}$–$5^{-4}) \lesssim 20$ ppm, which bounds the uncertainty in extrapolating to m_W to $b_3^2(5^{-4}$–$40^{-4})$ to 5 ppm.

As the impact of b_3 grows rapidly with curvature, the range of $|c|$ spanned by the $J/\psi \to \mu\mu$ data yields additional information on b_3. As mentioned above, the momentum calibration in the bins of largest $|c| \sim 0.43$ GeV^{-1} differs from the momentum calibration derived from the remainder of the bins (whose typical $|c| \sim 0.3$ GeV^{-1}) by 20 ppm [2]. This implies that $b_3^2(0.43^4$–$0.3^4) \lesssim 20$ ppm, which bounds the uncertainty in extrapolating to m_W to $b_3^2(0.3^4$–$40^{-4})$ to 6 ppm.

As with the bounds on a_3, the J/ψ and Υ data shown in Ref. [2] exert pulls on b_3 in opposite directions; their average yields a vanishing value of b_3, with a negligible uncertainty of 4 ppm. When combined with the constraint from the

cosmic-ray data of 5 ppm, the uncertainty due to b_3 reduces further to 3 ppm.

3. Summary of a_3 and b_3

The quoted uncertainty of 25 ppm on m_W ascribed to the momentum calibration includes the potential uncertainty of 12 ppm from a_3, and the uncertainty due to b_3 is negligible.

V. APPLICATION TO THE m_W MEASUREMENT

In the $p\bar{p}$ collisions at the Tevatron, the beams of equal energy produce W^+ and W^- bosons with identical momentum distributions except for a longitudinally antisymmetric component due to the CP-invariant initial state. The antisymmetric component of Δ_{pe} is discussed and incorporated into the m_W analysis [2]. Taking advantage of the ensuing symmetries in the charged lepton distributions, as well as the longitudinal and azimuthal symmetry in the construction of the COT, we exploit the identity of the response function for both charges.

A. First-order bias in m_W

The W boson mass is extracted from a fit to the p_T distribution of the charged lepton, or to the distribution of transverse mass or p_T^{ν}. The latter depend also on the calibration of the hadronic recoil vector, which is calibrated using the tracker as reference. Thus, we can consider $m_W \propto p_T \propto q/c$ and the first-order fractional bias in the W boson mass is

$$\frac{-\delta m_W}{m_W} = q\frac{\delta c}{c^2}\frac{c}{q} = \frac{\delta c}{c} = \frac{a_0}{c} + (a_1 + b_1 q) + (a_2 + b_2' q)c + (a_3 + b_3 q)c^2,$$

where the ϵ^2 term is accounted for in the m_W measurement with vanishing uncertainty and therefore dropped.

Consider the half-difference of $\frac{\delta m_W}{m_W}$ between W^- and W^+ bosons,

$$\begin{aligned}\Delta_W^{\mp} &\equiv \frac{-1}{2}\Sigma_q q\frac{\delta m_W}{m_W} \\ &= \frac{1}{2}\Sigma_q q\left[\frac{a_0}{c} + (a_1 + b_1 q) + (a_2 + b_2' q)c + (a_3 + b_3 q)c^2\right] \\ &= \frac{1}{2}\Sigma_q\left[a_0 p_T + b_1 + a_2 p_T^{-1} + b_3 p_T^{-2}\right] \\ &= a_0 p_T + b_1 + a_2 p_T^{-1} + b_3 p_T^{-2} = B, \end{aligned} \tag{7}$$

since $a_1\Sigma_q q$, $b_2'\Sigma_q c$ and $a_3\Sigma_q q c^2$ vanish by charge symmetry. This expression is identical to Δ_{pe} shown in Sec. III. As the median p_T and the Jacobian edge of the p_T distribution are similar within a few GeV, $\Delta_W^{\mp}$ is calibrated away by the constraint from Δ_{pe}, the positron-electron difference of $\langle E/p\rangle$. As expected, the charge-antisymmetric terms in B [Eq. (6)] provide the causal explanation for the $\Delta_W^{\mp}$ observable.

We consider the average of $\frac{\delta m_W}{m_W}$ for W^+ and W^- bosons, which reflects a first-order bias in m_W,

$$\frac{1}{2}\Sigma_q\frac{\delta m_W}{m_W} = \frac{1}{2}\Sigma_q\left[\frac{a_0}{c} + (a_1 + b_1 q) + (a_2 + b_2' q)c + (a_3 + b_3 q)c^2\right] = a_1 + b_2' p_T^{-1} + a_3 p_T^{-2} = A,$$

because $a_0\langle c^{-1}\rangle$, $b_1\Sigma_q q$, $a_2\langle c\rangle$ and $b_3\langle q c^2\rangle$ vanish by charge symmetry. As expected, the charge-symmetric terms in A [Eq. (5)] induce an m_W bias.

As mentioned in Sec. IV, b_2' is constrained to within 34 keV, hence its contribution to a first-order bias in m_W is negligible ($b_2'\langle p_T^{-1}\rangle \sim \frac{34\,\text{keV}}{35\,\text{GeV}} \sim 1$ ppm). The momentum scale parameter a_1 has been calibrated to 25 ppm [2], which includes a potential uncertainty due to a_3 of 12 ppm. We conclude that the analytic curvature response function, expanded up to c^3 terms, is sufficiently well-constrained to prevent significant first-order bias in m_W.

B. Second-order bias in m_W

Extending the derivative to second order,

$$\frac{\delta m_W}{m_W} = q\frac{(\delta c)^2}{c^3}\frac{c}{q} = \left(\frac{\delta c}{c}\right)^2,$$

which after calibration (i.e., dropping the a_1, b_2' and ϵ^2 terms) simplifies to

$$\begin{aligned}\frac{\delta m_W}{m_W} &= (a_0 c^{-1} + b_1 q + a_2 c + a_3 c^2 + b_3 q c^2)^2 \\ &= \left(a_0 p_T + b_1 + a_2 p_T^{-1} + b_3 p_T^{-2} + a_3 q p_T^{-2}\right)^2 \\ &= \left(\Delta_W^{\mp} + a_3 q p_T^{-2}\right)^2 \\ &= (\Delta_W^{\mp})^2 + \left(a_3 p_T^{-2}\right)^2 + 2q(\Delta_W^{\mp})\left(a_3 p_T^{-2}\right).\end{aligned}$$

The quantity $\Delta_W^{\mp} = (m_{W^-} - m_{W^+})/m_W$ is measured to be consistent with zero within a statistical precision of 0.2‰ [2]; therefore, the first term is 0.04 ppm based on this measurement. If Δ_{pe} is used instead of $\Delta_W^{\mp}$, then the constraint has a statistical precision of $(43\text{ ppm})^2 = 0.002$ ppm which is tighter by another order of magnitude. As mentioned in Sec. IV B 1, the constraints from $\Delta_W^{\mp}$ and Δ_{pe} apply mostly to the low-curvature parameters a_0 and b_1; this is reflected in Table I.

The term $a_3 p_T^{-2}$ is constrained to 12 ppm from the J/ψ and Υ data; hence, the square of this term is vanishing.

The third (product) term is charge-dependent, of $\mathcal{O}(2 \times 0.2‰ \times 34\,\text{ppm}) \sim 0.01$ ppm or smaller, which is vanishing.

We conclude that the second-order bias on m_W can be estimated from the constraints on the parameters in the COT response function, from the measurement of $\Delta_W^{\mp}$, and from the calibration based on Δ_{pe}. All estimates are vanishingly small.

C. Summary of analytic curvature response function

The parameters of the analytic curvature response function [Eq. (1)] propagate to the momentum calibration uncertainty on m_W at first or second order. Based on cosmic-ray data and the published J/ψ and Υ data [2], all uncertainties are either already included in the m_W analysis [2] or found to be negligible.

As mentioned earlier, the CDF procedure to calibrate track p_T is based on mass measurements of the J/ψ and Υ mesons in the dimuon channel [2,3,24]. These data samples are binned in the mean $|c|$ of the two muons and mass fits are performed in each bin separately. An inclusive mass fit is also performed for the Υ sample. The mass fits are based on

TABLE I. The constraints obtained from independent datasets on the a_n and b_n parameters of the curvature response model [Eq. (1) and Sec. VI B 3]. The constraints are presented in terms of the corresponding uncertainty (in ppm) on the W boson mass. Note that $b'_2 \equiv b_2 + \epsilon$ where ϵ is the energy loss incurred by a muon as it traverses the tracker. The half-difference of $\langle E/p \rangle$ between positrons and electrons in $W \to e\nu$ decays is denoted by Δ_{pe} as shown in Eq. (4). The fractional half-difference in m_W between positive and negative leptons is denoted by $\Delta_W^{\mp}$ as shown in Eq. (7). The numbers in parentheses refer to the section of this document where the corresponding details are provided. The $\mathcal{I}$ entries indicate parameters that are invisible to the corresponding observables. The $\mathcal{N}$ entries indicate parameters that are not constrained by the corresponding observables. Note that the constraint on a_1 from the $J/\psi \to \mu\mu$ and $\Upsilon \to \mu\mu$ data already takes into account the effects of the b'_2, a_3, and b_3 parameters in the quoted 25 ppm uncertainty [2].

Dataset	a_0	b_0	a_1	b_1	a_2	b'_2	a_3	b_3
Cosmic rays	0.2 (IV B 1)	0.005 (VI C)	$\mathcal{I}$ (II B)	0.3 (IV B 1)	0.008 (IV B 1)	$\mathcal{I}$ (II B)	$\mathcal{I}$ (II B)	0.003 (IV B 1)
$J/\psi, \Upsilon \to \mu\mu$	$\mathcal{N}$ (IV A)	$\mathcal{N}$ (IV A)	25 (I)	$\mathcal{N}$ (IV A)	$\mathcal{N}$ (IV A)	1 (IV A)	12 (IV C 1)	4 (IV C 2)
$\Delta_W^{\mp}$ $(W \to \ell\nu)$	0.04 (V B)	$\mathcal{I}$ (V A)	$\mathcal{I}$ (V A)	0.04 (V B)	$\mathcal{N}$ (V B)	$\mathcal{I}$ (V A)	$\mathcal{I}$ (V A)	$\mathcal{N}$ (V B)
Δ_{pe} $(W \to e\nu)$	0.002 (V B)	$\mathcal{I}$ (III)	$\mathcal{I}$ (III)	0.002 (V B)	$\mathcal{N}$ (V B)	$\mathcal{I}$ (III)	$\mathcal{I}$ (III)	$\mathcal{N}$ (V B)

likelihood maximization using simulated templates for the signal line-shapes. The background shapes are modeled and their normalizations are constrained using the sidebands of each mass peak in the data. The simulation models meson/boson production and decay and the propagation of muons (and electrons) through the detector, including energy loss and resolution effects. The mass bias δm is defined as the difference of the measured meson mass from the world-average reference (particle data group) value.

We have shown that the fractional mass bias $\delta m/m$ as a function of $|c|$ is parameterized in general by the A terms [Eq. (5)] at first order, and by B^2 [Eq. (6)] at second order. We have also shown that B^2 is strongly constrained to be zero by both the cosmic-ray analysis and by Δ_{pe}, the positron-electron difference of E/p [Eq. (4)]. Since they contribute negligibly, the B^2 terms can be dropped in subsequent analysis and only the A terms need to be extracted. Furthermore, since the a_3 term in A is redundant within the quoted uncertainties on a_1 and b'_2, it is appropriate to let $a_3 = 0$ and extract a_1 and b'_2 from a linear fit to $\delta m/m$ versus $|c|$, as shown in Fig. 2(A) of Ref. [2], Fig. 13 of Ref. [24], and Fig. 22 of Ref. [3]. In practice, the energy loss ϵ is tuned in the simulation by a few % of its *ab initio* value such that the linear fit returns $b'_2 = 0$. Therefore, these figures in the respective publications display the value of a_1 corresponding to the as-built detector and track reconstruction software, i.e., prior to final calibration of track p_T at the analysis level.

We note that the four points from $J/\psi \to \mu\mu$ data at small $|c|$ in Fig. 2(A) of Ref. [2], if combined, would deviate from the model by 2σ. The large number of points that are consistent with the model, together with the stringent constraints on the model from multiple independent control samples of data, preclude nonlinear models. In order for these points to be indicative of a systematic effect, the model must include the B^2 term of the form $(a_0 p_T)^2 = (a_0/c)^2$. We have shown that this term has been eliminated by the high-quality alignment, both internal and external, of the COT, and by the Δ_{pe} constraint. Furthermore, this term has negligible impact in the range of $|c|$ where the J/ψ and Υ data constrain a_1. Hence, the extraction of a_1 from the J/ψ and Υ data using the linear fit to $\delta m/m$ versus $|c|$ is robust. There is no justification for a nonlinear fit, given the preponderance of evidence against it, merely to accommodate a fluctuation.

These procedures lead to the inference that $\delta m/m = a_1$ for all resonances. CDF developed these procedures to constrain a_1 from the J/ψ and Υ data and apply it to calibrate the p_T of tracks from W and Z boson decays at the analysis level. The uncertainties due to b'_2 and a_3 have been included in the quoted uncertainty on a_1, and we have shown that all other terms in the curvature response function [Eq. (1)] are negligible. Thus, the most general analytic response function is completely pinned down.

VI. SINGULAR CURVATURE RESPONSE FUNCTIONS

Equation (1) shows the analytic response function for curvature as a Maclaurin expansion, appropriate for the $W^{\pm}$, Z, Υ, and J/ψ samples which have symmetric c distributions about $c = 0$ at the Tevatron.[8] Since tracking detectors measure curvature, the coefficients of the response function relate to the geometry and the physics principles on which the hit measurements are based.

A. Terms with negative exponents

One may consider extending the response function from an analytic Maclaurin series to a nonanalytic Laurent series by adding terms of the form $c^{-|n|}$ for integer values of n. Such terms must be forbidden on physical grounds; as $c \to 0$ they imply $\delta c \to \infty$ which means that the particle's straight-line trajectory becomes indeterminate. Equivalently, such terms are inconsistent with the simple fact that if the axial magnetic field were ramped down to zero magnitude, $B_z \to 0^{\pm}$, all trajectories tend to straight lines which can easily be reconstructed by the drift chamber with no loss of directional information.

[8]The leptons from W boson decays do not have symmetric c distributions at the LHC.

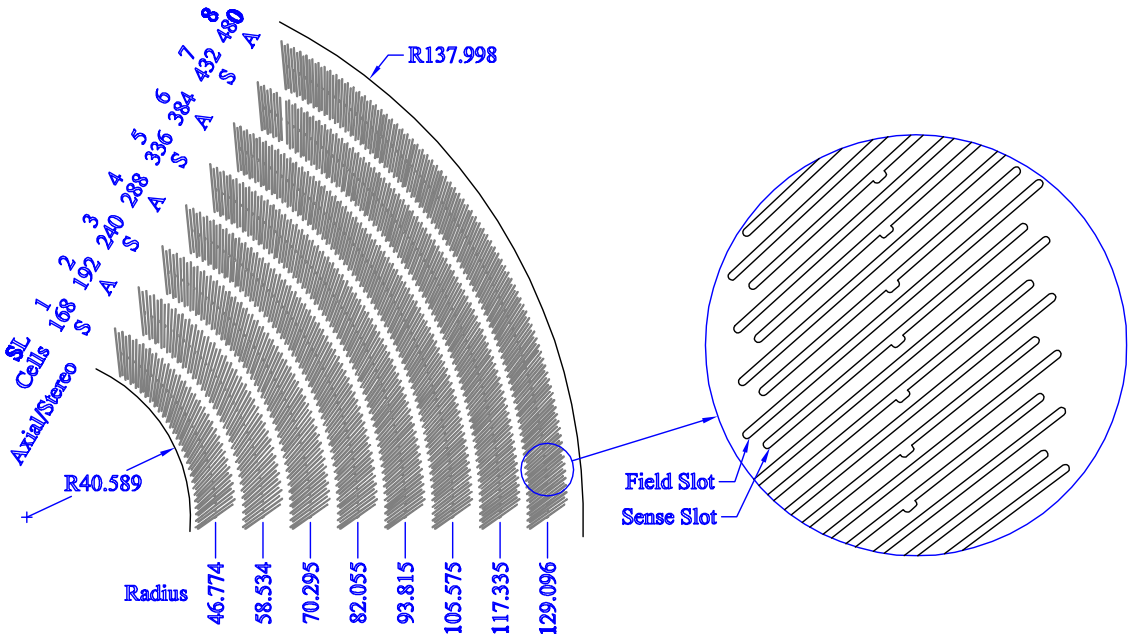

FIG. 4. End view of a section of the CDF COT end plate. The sense wires are organized into eight concentric "superlayers." Each superlayer is partitioned azimuthally into cells, and each cell contains 12 sense wires separated from adjacent cells by field sheets. Precision-machined slots in the end plates hold each cell's sense wires and field sheets under tension. The radius at the center of each superlayer is shown in cm. Figure reproduced with permission from Fig. 2 of Ref. [1].

Figure 4 shows the physical construction of the COT [1]. It is a single, cylindrical gaseous volume in which sense wires and field sheets are embedded. The only way for a particle trajectory to be indeterminate is if the particle were to traverse an uninstrumented region of the tracking volume. As $c \to 0$ the particle trajectories approach a straight line in the radial direction. All sense-wire and field-sheet planes are tilted (at 35°) with respect to the radial direction in an azimuthally symmetric manner [1]. With this construction, there is no dead space that the particle can traverse; the entire volume is active. There are no azimuthal boundaries through which a particle may pass without ionizing gas adjacent to every sense wire. Hence, every radial straight line is detectable as such.

1. COT performance studies with cosmic rays

As described in Sec. II, the cosmic-ray sample is collected in situ with collider data using the high-p_T inclusive muon trigger that also acquires the $W \to \mu\nu$ and $Z \to \mu\mu$ data. The sample can therefore be used to study the COT performance under the same operating conditions as the physics signals.

The fraction of the maximum possible number of COT hits contributing to cosmic-ray tracks is shown in Fig. 5. As the track tends to a straight line, the fraction of hits associated with the track increases slightly, by 1‰, because pattern recognition becomes easier as the curvature reduces. Importantly, there is no indication of a loss of performance or efficiency in the $c \to 0^{\pm}$ limit.

The typical alignment accuracy of the wires is 1 μm [2,21]. Even if we make the extremely conservative assumption that the change in efficiency is due to one particular wire which induces a curvature bias of $\mathcal{O}(1\,\mu\text{m}/l^2)$, where $l \sim 1$ m is the length of the track, this bias would amount to 0.2 ppm at $m_{W,Z}$ (see Appendix F for the calculation). Furthermore, as a (signed) curvature bias, it cancels at first order in sign-averaged mass measurements and would be vanishing at second order. To induce a first-order bias, there would need to be a difference in this inefficiency variation between positive and negative particles. As seen in Fig. 5, the difference between positive and negative tracks is much smaller than 1‰. We conclude that the high degree of stability of the hit efficiency (pattern recognition) with respect to curvature, together with the accurate alignment, supports the ansatz that the COT has no discernible discontinuity in the $c \to 0^{\pm}$ limit.

Another performance metric is the fraction of superlayers that contribute to the track (see Fig. 5), where a superlayer is counted if it contributes at least 5 of the maximum 12 hits. This criterion is the one used in the m_W analysis for candidate track selection [2]. The superlayer fraction is $\varepsilon = 999.5‰$, independent of curvature as $c \to 0^{\pm}$ and reduces by $\Delta\varepsilon = 0.2‰$ for p_T values below the selection criterion used for W and Z boson samples [2]. This metric is the most relevant for the curvature response function and indicates that the COT performance is independent of curvature in the $c \to 0$ limit.

In Fig. 5 (right), the parameter κ is designed to capture any charge-dependent superlayer efficiency as $c \to 0^{\pm}$. We find that κ is zero within a statistical precision of 0.04‰, strongly disfavoring any discontinuous behavior.

In Appendix F we also estimate the possible mass bias induced by the superlayer inefficiency, and arrive at a more realistic bound of 4 ppb, based on a maximum superlayer efficiency variation of 0.1‰ in the $c \to 0^{\pm}$ limits.

The stability of the COT performance with respect to time is demonstrated in Fig. 6. To interpret time stability in the context of collider data, hit and superlayer efficiencies are presented in sequential blocks of integrated luminosity. Fig. 6

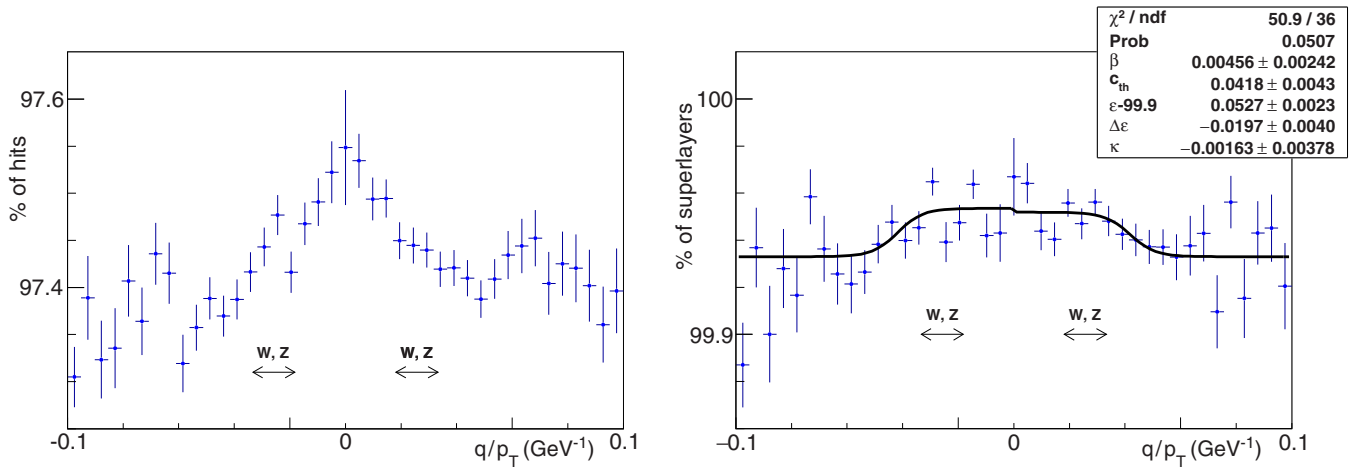

FIG. 5. (Left) The fraction of the maximum possible number of COT hits contributing to the cosmic-ray tracks. (Right) The fraction of the maximum possible number of superlayers contributing to the cosmic-ray tracks, when a superlayer is required to contribute at least 5 (of 12) hits. The fit is intended to guide the eye. The superlayer efficiency is constant at 99.95% at low curvature and lower by 0.02% for $|c_{\rm th}^{-1}| = p_T \lesssim 25$ GeV when a different trigger is used. The fit function is $y = \varepsilon + \Delta\varepsilon/(1+e^{-\xi}) + \frac{q}{2}\kappa/(1+e^{\xi})$ where $\xi = (|x| - |c_{\rm th}|)/\beta$. The parameter $\kappa = (0.002 \pm 0.004)\%$ describes the difference in superlayer efficiency as $c \to 0^+$ versus $c \to 0^-$.

shows that the hit efficiency actually increased after 2007, when 3/4 of the data were collected, and remained remarkably stable post-2007, with a worst-case drop of 1.5‰. The superlayer efficiency is even more stable due to the inherent redundancy in the requirement of 5-of-12 hits per superlayer. This inefficiency is consistent with a constant value of 520 ± 30 ppm over the 10-year operation of the COT, proving that there is little evidence for degradation or radiation damage and no visible impact on tracking efficiency.

Stability with respect to instantaneous luminosity, i.e., occupancy is provided by the COT track reconstruction procedure. After the first pass of pattern recognition, hit association and track-fitting, a second-pass refit of COT tracks is performed. Prior to this refit, hits whose distance from the track exceeds a threshold of about 4× the hit resolution are removed from the track. Next, unused hits whose distance from the track is less than about 3× the hit resolution are added to the list of associated hits. The updated hit list is refitted to obtain the track parameters used for analysis. This "drop-add" procedure removes spurious hits and rescues hits that were missed in the first-pass reconstruction due to high occupancy. Together with the high level of redundancy in the COT tracker (up to 96 hits per track), the procedure makes COT tracks robust, stable and insensitive to occupancy.

2. *Summary of performance studies and negative-exponent terms*

By design, the COT geometry is continuous, without boundaries, and is sampled uniformly by tracks in the $c \to 0^{\pm}$

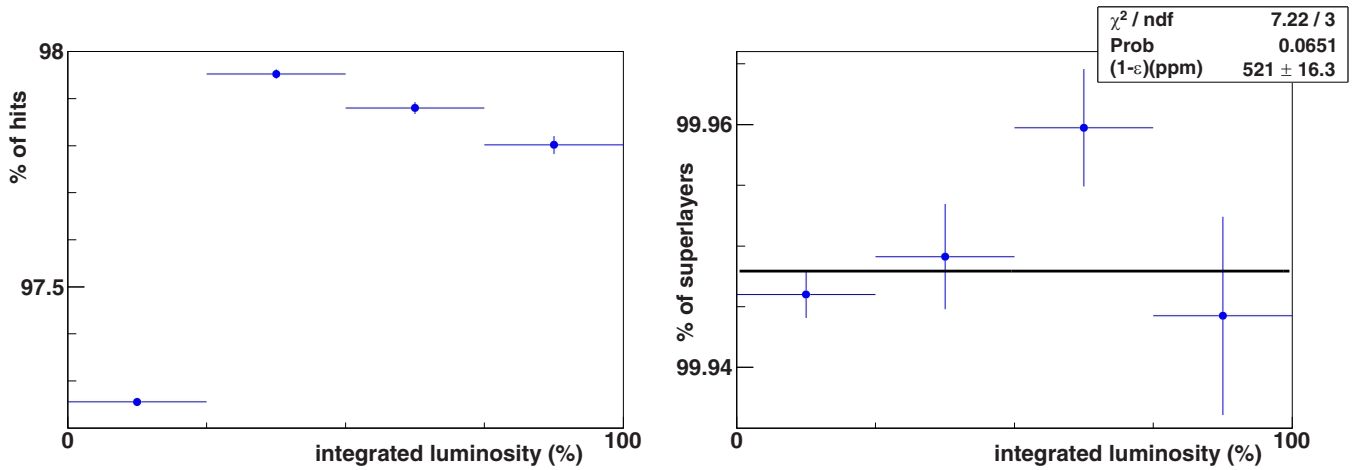

FIG. 6. (Left) The fraction of the maximum possible number of COT hits contributing to the cosmic-ray tracks. (Right) The fraction of the maximum possible number of superlayers contributing to the cosmic-ray tracks, when a superlayer is required to contribute at least 5 (of 12) hits. The fractions are shown in four sequential time periods, with each period delivering a quarter of the total integrated luminosity recorded by CDF II and used for the m_W measurement [2]. The superlayer inefficiency is consistent with a constant value of (520 ± 30) ppm over the entire 10-year operation of the COT. For these data, the requirement $p_T > 20$ GeV is imposed to be applicable to the W and Z boson data. The complementary sample with $10 < p_T < 20$ GeV shows similarly stable efficiencies at slightly lower values, as seen in Fig. 5.

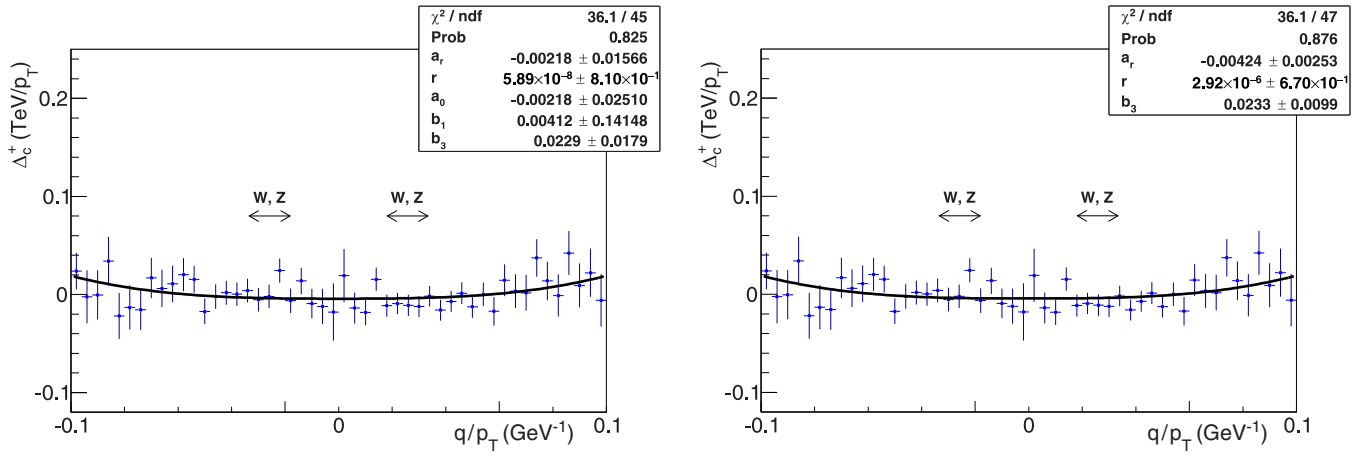

FIG. 7. (Left) The measurement of Δ_c^+ as a function of c_d, the measured curvature of the COT dicosmic helix, in cosmic-ray data collected in situ during collider operation. The requirement $|z_0| < 60$ cm ensures that the cosmic-ray tracks have similar trajectories as the particles selected for physics analysis. The data have been corrected for the known energy loss ϵ, same as in Fig. 3. Also shown is the fit to Eq. (2) including the $a_r|c|^r$ term ($0 < r < 1$), with the values and statistical uncertainties of the fitted parameters a_r, r, a_0 (in TeV^{-1}), b_1 (in ‰), and b_3 (in GeV^2). (Right) The same data and fit with a_r, r and b_3 as the fitted parameters. The error bars indicate the statistical uncertainties on the data points. The horizontal arrows indicate the range of q/p_T of the leptons originating from $W \to \ell^\pm\nu$ and $Z \to \ell^+\ell^-$ decays that are used in the m_W analysis [2].

limits. This reasoning eliminates terms of the form $c^{-|n|}$ and by extension, $c^{-|r|}$ for real values of r. Studies of hit efficiency and superlayer efficiency as a function of curvature support this reasoning at a more stringent level (by four orders of magnitude) than the uncertainty of 25 ppm on the momentum calibration quoted in Ref. [2].

B. Terms with fractional exponents

The Maclaurin series may be extended to a Puiseux series by including terms with fractional (positive) exponents. We consider terms with fractional positive powers of c in the response function. Since c is a signed quantity we must consider two types of terms, $|c|^r$ and $q|c|^r$, where $0 < r < 1$. In principle, such factors may multiply the entire analytic function of Eq. (1). However, the a_0, a_1 and ϵ terms have obvious physical interpretations and may not be altered.

The degrees of freedom incorporated in Eq. (1) already span the phase space of the calibration data. By the AIC we can use the minimal model that adequately describes the data, and propagate the uncertainties in the model parameters. Therefore, the additional terms of fractional powers are only needed to explore the $c \to 0$ limit.

We consider the terms $a_r|c|^r$ and $b_r q|c|^r$ individually, since they are even and odd in q, respectively.

1. Charge-independent term with fractional exponent

In Fig. 7 (left) we extend the fit of Fig. 3 to include the term $a_r|c|^r$. The fit finds $r = 0$ which means that this term is redundant with a_0; a conclusion confirmed by their mutual correlation coefficient of -97%. Also, the b_1 and b_3 terms are anticorrelated with a correlation coefficient of -88%. The a_0 and b_1 terms are dropped to increase the incisiveness of the fit; the χ^2/dof decreases as shown in Fig. 7 (right). This fit returns $r = 0^{+0.06}_{-0}$ which implies that the data do not differentiate this term from the a_0 term.

In Fig. 8 (left) we illustrate the function $|c/0.1|^{0.06}$ where the exponent is chosen to reflect the range compatible with the fit of Fig. 7 (right). This term is highly nondifferentiable at $c = 0$; the slope changes from $-\infty$ at $c = 0^-$ to ∞ at $c = 0^+$. It implies that zero curvature is distinguishable from vanishing curvature, a conclusion inconsistent with the fact that all drift distances in the COT change continuously with c for all relevant values of c. There is no physical model that generates such a fractional-exponent term.

Also shown in Fig. 8 (left) are two linear functions based on the a_0 and b_1 terms from Eq. (1). These linear functions are intended to guide the eye. One of these lines intersects $|c/0.1|^{0.06}$ at $|c| = 0.05$ GeV^{-1} and $|c| = 0.01$ GeV^{-1}, i.e., $p_T = 20$ GeV and 100 GeV which flank the range of the charged leptons from W and Z boson decays. The second line is tangent to $|c/0.1|^{0.06}$ at $p_T = 40$ GeV, typical for these leptons. The similarity of these linear functions to $|c/0.1|^{0.06}$ indicates that this function can be adequately approximated by Eq. (1) in the relevant p_T range; furthermore, the approximation improves as the exponent reduces.

We conclude that a charge-independent term with fractional exponent is excluded by the cosmic-ray data. It is also inconsistent with the known physical properties of the COT. In any case, the a_0, b_1, a_2, and b_3 terms provide a physically justifiable model that can adequately mimic any such effect in the relevant range of curvature.

2. Charge-dependent term with fractional exponent

We consider the extremes of the possible range $0 < r < 1$ of the exponent in the term $b_r q|c|^r$. As $r \to 1$ the term $b_r q|c|^r \to a_1 c$ and hence becomes redundant with the momentum scale. As $r \to 0$ the derivative of the response function near $c = 0$ diverges more rapidly as $|c|^{r-1}$. This is illustrated in Fig. 8 (right). We also have $\lim_{r\to 0} b_r q|c|^r = b_0 q$ so that the response function develops a discontinuous step

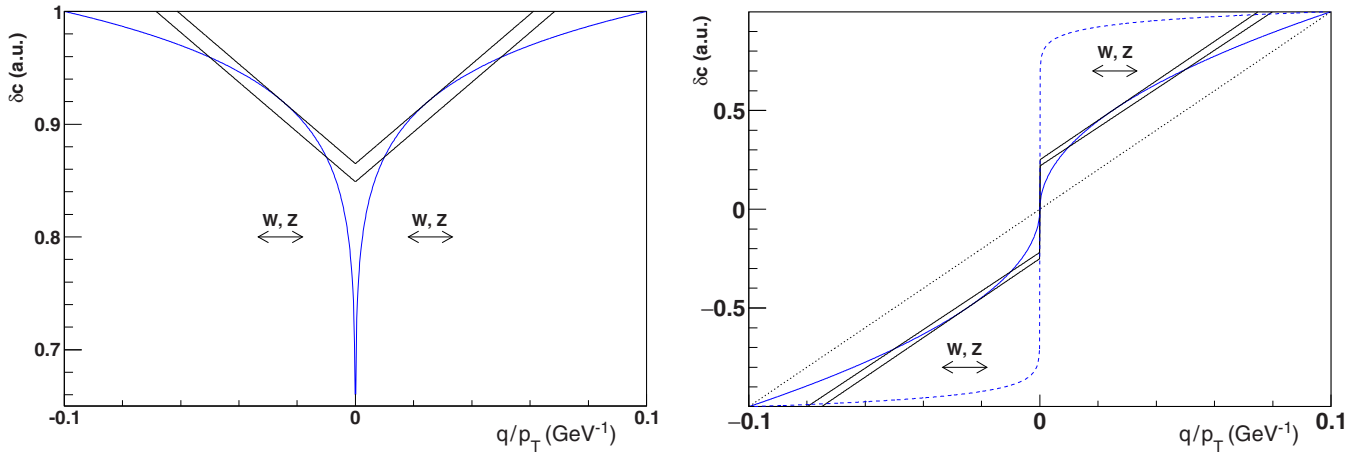

FIG. 8. (Left) An illustration of the function $|c/0.1|^{0.06}$ (solid blue curve). (Right) An illustration of the function $q|c/0.1|^r$ for $r = 0.5$ (solid blue curve), $r = 0.05$ (dashed blue curve), and $r = 1$ (dotted black line). In each illustration, two straight-line approximations are shown for the solid blue curve; a tangent at $p_T = 40$ GeV and a line that intersects the curve at $p_T = 10$ and 100 GeV. The linear approximations (solid black lines) indicate that a fractional exponent term can be mimicked by an intercept, a slope and higher-order terms in the relevant range of curvature.

function at $c = 0$. The implication is that a nearly straight track (with indeterminate q) is reconstructed with a false curvature whose sign depends on q. A physical explanation for such a response function of the COT is not plausible on the basis of its geometry and principles of operation, since the response cannot be insensitive to q and depend strongly on q at the same time.

3. *Effect of singular term on observables*

If the term $b_0 q$ is added to the response function of Eq. (1), then it cancels in the sum over the two legs of the cosmic ray and does not show up in Δ_c^+ [Eq. (2)]. It is shown in Appendix E 2 that Δ_c^- cannot constrain this term.

The effect of the b_0 term on Δ_{pe}, the positron-electron difference of $\langle E/p \rangle$ [Eq. (4)], and on $\Delta_W^{\mp}$, the mass difference between W^- and W^+ bosons [Eq. (7)], is vanishing,

$$\frac{1}{2}\Sigma_q q\frac{\delta c}{c} = \frac{1}{2}\Sigma_q q\frac{b_0 q}{c} = \frac{b_0}{2}\Sigma_q c^{-1} = \frac{b_0}{2}\Sigma_q q p_T = 0,$$

by charge symmetry.

The effect of the b_0 term on the reconstructed invariant mass is

$$\left.\frac{\delta m}{m}\right|_{1\text{st}} = \frac{-1}{2}\Sigma_q\frac{\delta c}{c} = \frac{-1}{2}\Sigma_q\frac{b_0 q}{c} = \frac{-b_0}{2}\Sigma_q\frac{q}{c}$$
$$= \frac{-b_0}{2}\Sigma_q p_T = -b_0\langle p_T\rangle.$$

Thus, any COT measurement bias that is mimicked by the $b_0 q$ term will result in biased m_W and m_Z measurements because it will not be calibrated by the J/ψ and Υ data at lower p_T.

4. *Study of discontinuous COT response*

As mentioned above, the $b_0 q$ term in the response function requires an unphysical discontinuity in the response as $c \to 0^{\pm}$. Since the entire gaseous volume is instrumented, a discontinuity would have to be generated by some feature of the electron drift. The drift cells are build to be almost mirror-symmetric (the plane of sense wires is half-way between the parallel planes of field sheets [1]), so the fraction of hits that involve leftward and rightward drifts are roughly equal. A small asymmetry between these fractions can be generated by the 35° supercell[9] tilt which compensates for the Lorentz angle in the magnetic field [1], and by the deflection of the wires due to the electrostatic forces from the field sheets [1,21].

Related to the left-right drift asymmetry is the average displacement of the hits from the sense wires. For exactly left-right symmetric drift, the average hit distance from the sense wire would be equal in both directions, thereby canceling in the average displacement.

Of interest to this study is the dependence of these cell-level diagnostics on the track curvature. Again, we use the dicosmic helix to provide the most precise and accurate measurement of the curvature $c_{\rm d}$ of the cosmic-ray muons. The left-right asymmetry and the average drift displacement for all cells is shown as a function of $c_{\rm d}$ in Fig. 9. In each case we fit for four parameters using the following linear function of $|c_{\rm d}|$ (in GeV^{-1}), $y_0 + q\delta_0/2 + 10|c_{\rm d}|(s + q\delta_s/2)$, with an explicit dependence on charge included. Thus, δ_0 captures any discontinuity in the $c \to 0^{\pm}$ limits and δ_s captures any charge-dependence in the slope as one approaches these limits.

The charge-independent geometrical effects of the COT geometry are captured by the y_0 and s parameters that describe these $p_T > 10$ GeV data. The drift-direction asymmetry and the average drift displacement provide consistent descriptions of the cell drift where the maximum drift distance is 8.8 mm [1]; multiplying this maximum distance by the directional asymmetry yields predictions for the average displacement that are consistent with the observed values of the latter. This consistency implies that the drift speeds are the same on both sides of the drift cell.

[9] A supercell consists of 12 drift cells, with each cell containing one sense wire.

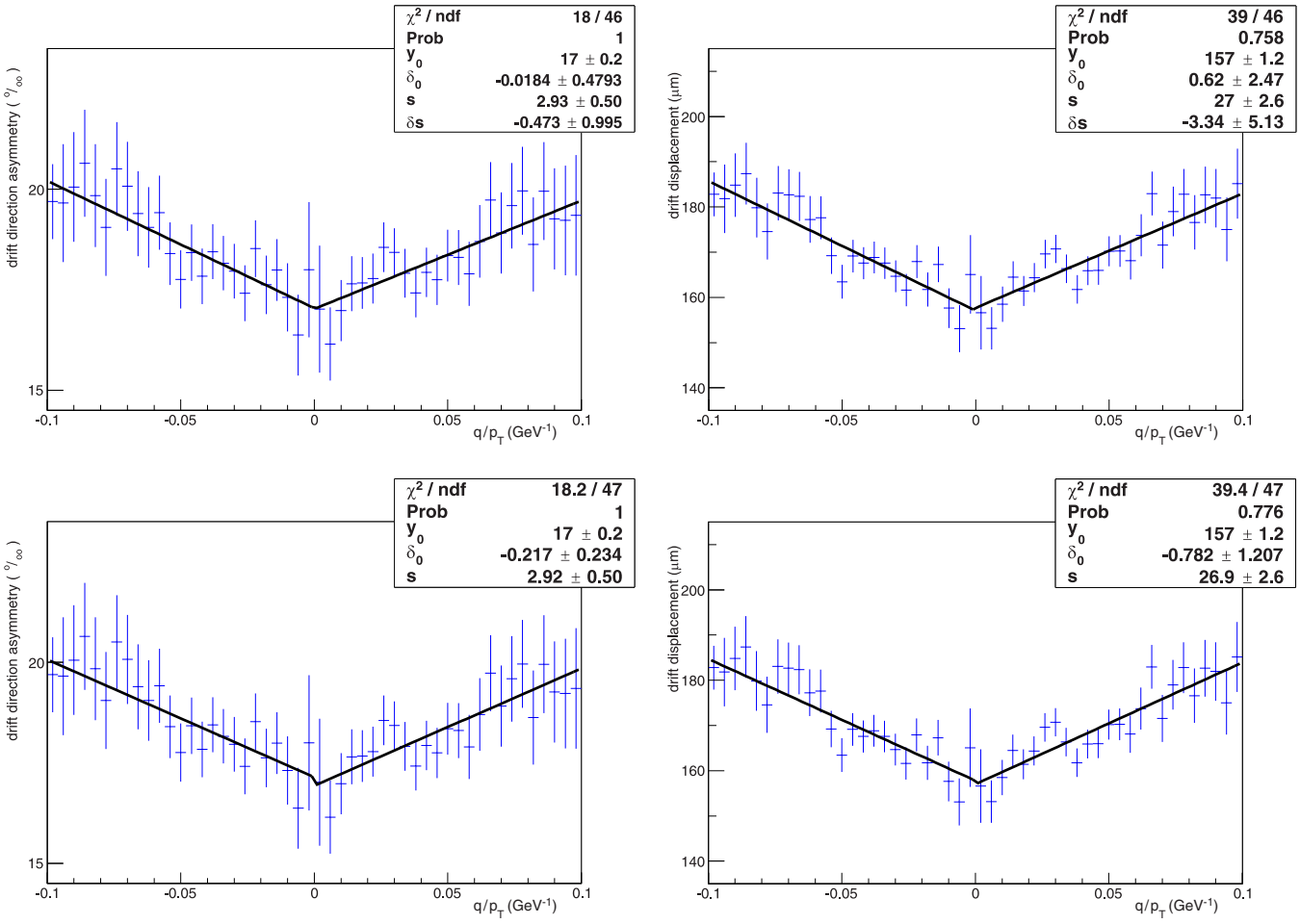

FIG. 9. Measurements of drift-cell properties using cosmic-ray data. (Left) The asymmetry between the fraction of hits drifting left versus right in each drift cell. (Right) The average drift displacement for all hits. (Top) The data are fit with the functional form $y_0 + q\delta_0/2 + 10|c|(s + q\delta_s/2)$ where c is in GeV^{-1}. (Bottom) The fit is repeated to the same data with the constraint $\delta_s = 0$.

The δ_0 and δ_s values are consistent with zero and do not support the hypothesis of a $b_0 q$ term. Since these parameters are strongly anticorrelated, the fit is repeated with the constraint $\delta_s = 0$, i.e., the slope is taken to be charge-independent. This improves the χ^2/dof and the constraining power on δ_0, the parameter that tests for a discontinuity in the high-p_T limit. We find no discontinuity within a precision of 1.2 μm.

In Appendix F a hypothetical charge-dependent alignment bias of 1 μm is used to estimate an m_W bias of 4 ppb. Thus, the above constraint on δ_0 implies a bound of 5 ppb on any m_W bias.

A simulation of the COT geometry and drift cells can be used to explore potential sources of a $b_0 q$ term; currently no physical model for this term can be created. In Appendix G we present an energy-loss model as an illustration of an effect that generates this term, albeit with a vanishing value of the b_0 coefficient.

C. Summary of singular response functions

A nonanalytic response can be parameterized by terms of the form $(a_r + qb_r)|c|^r$ where r is not a whole number. All such terms imply discontinuities (gaps in acceptance or anomalous charge drift) that are inconsistent with the construction of the COT. We have demonstrated this fact by studying the hit efficiency and the drift displacement versus curvature, and showing that both observables vary extremely smoothly as $c \to 0^{\pm}$. The upper bound on any discontinuity in each observable corresponds to a systematic uncertainty on the momentum calibration of 5 ppb.

We have shown that a nonanalytic response is adequately captured by a term of the form $\delta c = b_0 q$ to parametrize a discontinuity as $c \to 0^{\pm}$. We show in Appendix G that synchrotron radiation induces this term with a momentum miscalibration of 0.0001 ppb.

VII. SUMMARY

We have discussed a curvature response model for the COT, the CDF experiment's drift chamber that operated during Run 2 of the Tevatron. In the preceding sections we have described how the model parameters a_n and b_n ($n = 0, 1, 2, 3$) capture the degrees of freedom relevant for calibrating the curvature response in the context of the m_W measurement. The constraints on these parameters have been derived from cosmic-ray alignment data collected in situ with collider data, as well as the E/p ratio of positrons and electrons from $W \to$

TABLE II. The constraints obtained from cosmic-ray data on a subset of the a_n and b_n parameters of the curvature response model [Eq. (1) and Sec. VI B 3]. The constraints are presented in terms of the corresponding uncertainty (in ppm) on the $m_{J/\psi}$ and m_Υ analyses; these constraints can be interpreted as the corresponding uncertainties on the a_1 extracted from the J/ψ and Υ data. The remaining parameters, b_2' and a_3 have already been accounted for in the quoted 25 ppm uncertainty on a_1 [2]. The columns labeled "Sec." refer to the section of this document where the corresponding details on the preceding columns are provided.

Analysis	a_0	b_1	a_2	b_3	Sec.	b_0	Sec.
$m_{J/\psi}$	0.001	0.3	0.8	5	IV B 3	<0.001	VI C
m_Υ	0.003	0.3	0.4	1	IV B 2	<0.001	VI C

$e\nu$ decays, and the $J/\psi \to \mu\mu$ and $\Upsilon \to \mu\mu$ data. These and other measurements over-constrain the model parameters and bound the systematic uncertainty on m_W, as summarized in Table I.

Table I reiterates the conclusion from Sec. V C that the analytic model of Eq. (1) is highly constrained by the combination of the datasets. In particular, the analytic parameters that contribute the largest momentum calibration uncertainty on m_W are already accounted for in the analysis of the J/ψ and Υ data. All other parameters contribute negligibly to the uncertainty on m_W.

We also considered the impact of all parameters on the $m_{J/\psi}$ and m_Υ analyses. Table II summarizes the constraints from cosmic-ray data and their impact on the momentum scale parameter a_1 extracted from the J/ψ and Υ data. Table II reiterates the conclusion from Sec. V C that the momentum calibration is robust with respect to analytic deformations of the COT.

Finally, a detailed analysis of nonanalytic response functions has been performed. It is shown that such functions imply a discontinuity as $c \to 0^{\pm}$ which is adequately captured by a term of the form $\delta c = b_0 q$. Cosmic-ray data are used to study the smoothness of the COT efficiency and drift displacement in the $c \to 0^{\pm}$ limit and the systematic uncertainty on m_W is constrained to 5 ppb due to any discontinuity. This is noted in Tables I and II. Cosmic-ray data also show that the COT efficiency is extremely stable in time; the superlayer inefficiency is consistent with a constant value of (520 ± 30) ppm over its entire 10-year operation.

Having considered a general curvature response model, we find that all parameters are tightly constrained by control samples of in-situ cosmic-ray data, J/ψ and Υ data in the dimuon channel, and the charge-asymmetry of lepton p_T measurements. Uncertainties due to all other parameters are found to be negligible in comparison with the quoted uncertainty on the momentum calibration [2].

VIII. CONCLUSIONS

We have studied a parametric model for the curvature response of the CDF experiment's drift chamber, which provides the momentum measurement of charged particles. This investigation includes terms that are analytic in curvature as well as terms that capture nonanalytic behavior in the limit of vanishing curvature. The study includes in situ cosmic-ray data recorded by the CDF detector during collider operation, as well as information from the publications describing the measurement of the W boson mass.

We find that the analytic terms in the most general ansatz have well-defined physical interpretations. They are either constrained within the published uncertainties or contribute negligibly to the uncertainty on the momentum calibration. Furthermore, the analysis presented here on the basis of first principles shows how parameter uncertainties can be controlled and understood without recourse to black-box methodology such as machine learning or high-dimensional fitting.

We find no realistic model that would generate significant nonanalytic terms without violating the principles of operation of the drift chamber or the physics of particle interactions. Nonanalytic terms are further constrained by analysis of the cosmic-ray data.

Without loss of generality, uncertainties due to all other parameters are found to be vanishing in comparison with the quoted uncertainty on the momentum calibration in the CDF m_W measurement [2], demonstrating the explanability and robustness of these procedures.

This study provides a framework for further investigation of this drift chamber and the analyticity of the curvature response of tracking detectors in general. The topic is of relevance to high-precision measurements of observables such as the W boson mass and the weak mixing angle where accuracy of particle tracking is important, at future fixed-target and collider experiments. A gaseous detector with a single unfragmented active volume can be calibrated at the level of accuracy required to meet the goals of those experiments.

ACKNOWLEDGMENTS

We thank our colleagues on the CDF experiment at the Fermi National Accelerator Laboratory. We thank J. Bendavid, M. Boonekamp, D. Froidevaux, P. Grannis, H. Montgomery, J. Stark, and C. Young for helpful discussions. We are grateful to Fermilab for providing computing resources and we acknowledge the support of the Office of High Energy Physics, U.S. Department of Energy Office of Science (Grant No. DE-SC0010007).

APPENDIX A: CORRESPONDENCE OF CURVATURE RESPONSE MODELS

The curvature response model presented here generalizes Eq. (23) of Ref. [3],

$$\delta c = \epsilon_1 + \epsilon_2 c + \epsilon_3 c^2 + \epsilon_4 c^3,$$

with the correspondence $\epsilon_{n+1} \leftrightarrow a_n$ as used in Eq. (1) of this document. In this work we have extended the model to include the $b_n q$ terms.

As noted in Sec. IV A, the parameter b_2 and the ionization energy loss appear in combination as a sum when these models are applied to outgoing particles. The ionization energy loss is explicitly considered as a tunable parameter in all CDF publications, i.e., Eq. (27) of Ref. [3], Sec. VII B 3 of Ref. [24], and Sec. VI A of Ref. [2]. Therefore, the inclusion of b_2 in this work does not materially augment the model; the new parameters we have included are b_0, b_1, and b_3. More importantly, we have shown that, with the inclusion of these parameters, the model is fully generalized for $p_T > 2$ GeV.

In previous CDF II publications, models were introduced to capture the spatial variation of a_0 after the cosmic-ray alignment; in particular, Eq. (24) of Ref. [3] and Eq. (14) of Ref. [24] parameterize the dependence of our a_0 parameter on the azimuthal and polar angles. After those earlier CDF publications, the cosmic-ray alignment of the COT was considerably improved [21], as was the determination of the beam coordinates, and no further azimuthal variation was observed (as demonstrated in Ref. [21]). As a result, most of the parameters of Eq. (24) of Ref. [3] and Eq. (14) of Ref. [24] were no longer needed for the latest CDF publication of m_W (Eq. (S4) of Ref. [2]).

As explained in Appendixes D 2 and D 4, a small dependence on polar angle remains after the cosmic-ray alignment due to the residual inaccuracy of the wire-shape model. The same quadratic parameterization is used in all three CDF II publications to correct for this residual misalignment. The nomenclature A, B, C is used in Eq. (15) of Ref. [24] and in Eq. (S4) of Ref. [2] (where the values of A and C are displayed), while the correspondence $A \to a_0, B \to a_1, C \to a_2$ matches Eq. (24) of Ref. [3], for the parameters of the quadratic polar-angle dependence.

Thus, the symbols used in the earlier parameterizations to describe spatial variation of the alignment have no correspondence with the a_n, b_n notation used in this work to describe curvature-dependent effects.

APPENDIX B: GLOBAL COT ALIGNMENT

The COT is well-aligned with the solenoid axis and accurately aligned with the beam axis.

1. Mutual alignment of the COT and the beam axis

The consistency of the COT coordinate system and the location of the beam axis is important to eliminate bias when the COT tracks are constrained to the beam coordinates. This consistency is ensured using a large collection of COT tracks of high quality. Their two-dimensional impact parameter vectors with respect to the beam axis (as recorded in the database) is used to compute any shift between the COT coordinate system and the beam axis. The COT is then shifted in the track reconstruction software and the data are re-reconstructed to confirm that the mutual alignment is now perfect (at the submicron level) since there is no shortage of data for this procedure. Convergence is achieved typically in one iteration and a maximum of two iterations.

This alignment is performed in separate run blocks by first identifying relative shifts between the beam axis and the COT coordinate system over the entire 10 years of operation. The run blocks integrate data between occurrences of significant shifts. The procedure ensures submicron-level mutual alignment over the full collider dataset.

One of the benefits of this accurate mutual alignment is that prompt COT tracks can be constrained to include the beam spot of transverse size $\sim$30 μm in the track fit, which improves the curvature (and thereby momentum) resolution considerably. There is no benefit from including silicon vertex detector information in the track fit, because the incremental improvement in momentum resolution is marginal and the COT track resolution is already good enough to not limit any aspect of the m_W measurement [2].

2. Mutual alignment of the COT and the solenoid

The COT is mounted on the inside of the solenoid support structure. The time-of-flight detector is installed between the COT and the solenoid, leaving free space of $\mathcal{O}(1$ mm) between the detectors. This tolerance limits the relative displacement or tilt of the COT with respect to the solenoid axis.

The static magnetic field inside the solenoid varies smoothly according to Laplace's equation. The magnetic field has circular symmetry and cannot have a first-order transverse gradient near its axis. A small transverse displacement between the COT and solenoid axes cannot change the field near the axis at first order. Away from the axis any change in the field averages over azimuth to zero at first order. The longitudinal component of the magnetic field changes by the cosine of a tilt angle; as the latter is limited to $\mathcal{O}(1$ mm/1 m $\approx$1‰), B_z is affected at $\mathcal{O}(1$ ppm) which is negligible.

Miscalibration of the magnetic field can only scale the track p_T by a smooth spatial function which precludes singular behavior in the $c \to 0$ limit, i.e., it cannot introduce singular terms in Eq. (1). Furthermore, a_0, b_1, a_2, and b_3 [B terms in Eq. (6)] cannot be induced because the magnetic field affects both charges symmetrically. Any induced A terms [a_1, b_2, and a_3 in Eq. (5)] are calibrated using the J/ψ and Υ data (Sec. V C) modulo the small nonuniformity of the magnetic field which is not averaged identically by the J/ψ, Υ, W, and Z boson decays. The field nonuniformity versus polar angle (a small fringe-field miscalculation) is calibrated using the J/ψ data in the CDF m_W analyses [2,3,24] with an uncertainty due to differences between the spatial distributions of the decay muons in the various signal samples.

APPENDIX C: IONIZATION ENERGY LOSS FOR COSMIC RAYS

For a transverse energy loss ϵ, the measured curvature is $c^{\text{measured}} = q/(p_T - t\epsilon)$, where $t = +1(-1)$ for outgoing (incoming) particles. Defining $\zeta \equiv \epsilon/p_T = \epsilon qc$,

$$\delta c \equiv c^{\text{measured}} - c = \frac{q}{p_T - t\epsilon} - \frac{q}{p_T} = c\left(\frac{1}{1 - t\zeta} - 1\right)$$

$$= c\frac{t\zeta}{1 - t\zeta} \simeq ct\zeta(1 + t\zeta) = c(t\zeta + \zeta^2) = c(tq\epsilon c + \epsilon^2 c^2).$$

Therefore, the energy loss induces the correction terms $\epsilon c^2(tq + \epsilon c)$ in the measured curvature of the incoming and outgoing muons, respectively.

Hard scattering from the drift chamber wires introduce small discontinuities in the curvature of the tracks. The impact of hard scattering may be estimated using the Rutherford formula for the differential scattering cross section,

$$\frac{d\sigma}{d\Omega} = \left(\frac{Z\alpha}{4E_\mu \sin^2(\theta/2)}\right)^2 \approx \left(\frac{Z\alpha}{E_\mu \theta^2}\right)^2, \qquad \text{(C1)}$$

for a nucleus of atomic number Z, lepton energy E_μ and small scattering angle θ, where $\alpha = \frac{e^2}{4\pi} = 137^{-1}$ is the fine-structure constant for lepton charge e.

A 40 GeV lepton traversing a 1.4 T magnetic field produces a curvature of 53×10^{-6}/cm and a maximum sagitta of ≈9 mm in the COT. This curvature is mimicked by a hard-scattering angle of 13 mrad at the middle radius of the COT. Since any hard scattering will create a deflection that is uncorrelated with the sign of the lepton charge and its track curvature, the deflection angle will not bias the true curvature but will cause fluctuations around the true curvature. A deflection of 0.4 mrad, when projected on the transverse plane by a factor of $1/\sqrt{2}$, will contribute a resolution of ≈2% on the curvature. The intrinsic curvature resolution of the COT [10] at 40 GeV is 2%, therefore the impact of a 0.4 mrad deflection is similar to the intrinsic resolution.

The probability of a hard-scatter deflection larger than 0.4 mrad can be conservatively estimated by integrating the Rutherford scattering differential cross section, yielding the cross section

$$\sigma \approx \pi\left(\frac{Z\alpha}{E_\mu\theta}\right)^2 = \pi\left(\frac{74/137}{40,000\,\text{MeV} \times 0.0004}\right)^2$$
$$= \pi\left(\frac{74/(137\times 16)}{\text{MeV}}\right)^2 \approx \pi(6.7\,\text{fm})^2 \qquad \text{(C2)}$$

for a 40 GeV lepton scattering off a tungsten nucleus. The probability p of a hard scatter is given by $p = \sigma n d$ where n is the number density of scattering centers (atoms) and d is the thickness of the scattering layer. For a tungsten wire of 40 μm diameter [1] in the COT, $n = 6.4 \times 10^{22}/\text{cm}^3$ yields $p = \pi(6.7 \times 10^{-13}\,\text{cm})^2 \times (6.4 \times 10^{22}\,\text{cm}^{-3}) \times (40 \times 10^{-4}\,\text{cm}) = 0.36‰$.

Each sense wire sits in the middle of a drift region of width 2 × 8.8 mm. The probability of a particle hitting a specific wire is (40 μm)/(17.6 mm) = 2.3‰. The corresponding poisson probability of the hard scatter is 0.36‰ × 2.3‰ ≈1 ppm. Summing over the wires in the radial direction, the total probability of a hard scatter with $\theta > 0.4$ mrad in *any* wire is 0.2‰.

Repeating this analysis for different θ thresholds leads to the same conclusion. For example, lowering the threshold by 10× will increase the rate 100× to 2%, but these smaller-angle scatters will contribute to the intrinsic resolution in quadrature and increase the latter by only 1% of itself; the net effect will again be 0.2‰ on the resolution. If we raise the threshold by 10×, then these large-angle scatters can affect the momentum measurement by 20%; however, their rate of 2 ppm is lower than misidentification backgrounds from other sources by three orders of magnitude [2,3,24]. Finally, we note that coherent elastic scattering off the nucleus, per the Rutherford formula, dominates over incoherent, inelastic scattering; thus, the latter can also be ignored.

These estimates show that the probability of a hard scatter is so small that it modifies the intrinsic resolution at less than the permille level. Furthermore, the resolution is modeled using hit residuals measured for the muon tracks in $Z \to \mu\mu$ data [2]; thus, the model already subsumes the tiny contribution from hard scattering. The observed non-Gaussian tails in the hit residuals, which are caused by complexity of pattern recognition, are incorporated in the model [2]. The small non-Gaussian (power-law) tail due to hard scattering is also subsumed.

This is the reason that the COT track fit is a simple χ^2-minimizing fit. More sophisticated methods such as the Kalman filter are unnecessary for a tracking detector that is as transparent as the COT. Furthermore, the simplicity of the simple χ^2-minimizing fit provides the advantage that COT tracking is easy to simulate from first principles, which aids in its accurate calibration. This is one of the motivations for building a transparent gaseous tracker such as a drift chamber or a time-projection chamber at a future electron-positron collider, where the tracker must be calibrated with extreme accuracy for measuring precision electroweak and Higgs observables.

Pions, kaons, and protons undergo additional hard scatters in the COT due to hadronic interactions. The thickness of tungsten traversed on average through the entire COT is 18 μm or 0.3‰ of a nuclear collision length. This rather small probability of a hadronic interaction explains why the same simple χ^2-minimizing fit in COT tracking is used for all particles, leptons, and hadrons.

APPENDIX D: SPATIAL UNIFORMITY OF THE COT

Figures 2 and 3 show the post-alignment constraints from cosmic-ray data on the a_0, b_1, a_2 and b_3 parameters; only b_3 is statistically significant. Tables I and II show that b_3 has no impact on the m_W, $m_{J/\psi}$, and m_Υ analyses. Hence, the spatial variation of b_1, a_2 and b_3 is moot.

The a_0 term is directly induced by misalignments. This is clear from Eq. (1); if the cosmic-ray alignment were performed with zero magnetic field,[11] the cosmic-ray trajectories would be straight lines with zero curvature and only a_0 would be sensitive to misalignments. It is therefore natural to associate with the a_0 parameter the *a priori* dependence of the alignment on the azimuthal (ϕ) and polar (θ) angles. The zero-field situation is effectively mimicked by reweighting positive cosmic rays to obtain the sample average $\langle c \rangle = 0$.

[10] The resolution of beam-constrained COT tracks is $\delta(\text{GeV}/p_T) = 0.5‰$ [3].

[11] In order for the cosmic-ray alignment to be applicable to physics measurements, the cosmic-ray sample must be collected in situ with collider data at full solenoidal magnetic field. The COT drift cells are designed to operate at the corresponding Lorentz angle. The drift model would not be appropriate for zero magnetic field and the alignment derived with a different drift model may not be applicable for full-field operation.

TABLE III. A summary of the variability displayed by the pulls as a function of azimuth, z_0 and polar angle, respectively (reproduced from Figs. 20–25 of Ref. [21]). Each pull is defined by the comparison of the observable between the incoming and outgoing legs of the cosmic ray. Note that Δ_c^+ [Eq. (2)] is defined as half of the pull defined in Ref. [21]. The ϕ_0, d_0 and z_0 (t_0) observables denote the azimuthal angle, the impact parameter and the z position (time of occurrence), respectively, of the tracks at the point of closest approach to the beam axis. "Pre-" and "Post-" refer to prealignment and postalignment with the cosmic-ray procedure, and "RMS" refers to the RMS of inclusive distribution of the pull after alignment, i.e., the intrinsic resolution. The first three (next two) rows of observables describe the track's trajectory in the transverse plane (longitudinal view). The 8 ps bias in t_0 translates to an immaterial 0.4 μm effect using the drift speed of 50 μm/ns in the COT.

Pull	Azimuth		z_0		$\cot\theta$		
observable	Pre-	Post-	Pre-	Post-	Pre-	Post-	RMS
Δ_c^+ (PeV^{-1})	[−1200, 0]	±20	[−620, −580]	±40	[−800, −500]	±30	930
$\Delta\phi_0$ (μrad)	[−1400, 0]	±5	[−650, −500]	±15	[−600, −500]	±10	840
Δd_0 (μm)	[−400, 100]	±2	[−180, −160]	±8	[−230, −150]	±4	310
$\Delta\cot\theta$ (10^{-6})	[−4000, 3000]	±40	[−2500, −500]	±150	[−1600, −1200]	±50	4300
Δz_0 (μm)	[−3000, 3000]	±40	[−350, −250]	±30	[−400, −300]	±40	3800
Δt_0 (ps)	[−150, 300]	8 ± 8	[0,20]	[0,20]	[0,30]	[0,30]	430

Formally, the interplay between the a_n and b_n coefficients in the alignment procedure can be understood as follows. The positions of the supercells are adjusted to minimize the residuals with respect to the dicosmic fit [21]; as a consequence, the sample average $\langle\Delta_c^+\rangle$ is minimized. Equation (2) implies that the quantity $[a_0 + b_1\langle|c|\rangle + a_2\langle|c|^2\rangle + b_3\langle|c|^3\rangle]$ is minimized. We ignore the statistically insignificant coefficients b_1 and a_2. The $|c|$ distribution is approximately a Gaussian with mean 35 TeV^{-1} and RMS 25 TeV^{-1}, thus $\langle|c|^3\rangle \sim 110\,000$ TeV^{-3}. Using $b_3 \sim 0.022$ GeV^2 from Fig. 3 yields $b_3\langle|c|^3\rangle \sim 2.5$ PeV^{-1}. Thus, the effect of b_3 is much smaller than the statistical uncertainty of 10 PeV^{-1} on a_0 and can be ignored; spatial uniformity needs to be addressed in the context of a_0 only.

1. Benefits of symmetry and continuity

The simplicity of the COT geometry and its azimuthal (Fig. 4) and longitudinal symmetries limit the *a priori* spatial variation of the a_0 parameter. Table III shows that this variability is similar to the intrinsic resolution.

The longitudinal symmetry is broken by the deviation of the wires' shape from a straight line due to electrostatic deflection and gravitational sag. Nevertheless, only a handful of parameters are required to describe the shape analytically; it must be a smooth, quadratic function of $|z|$ at static equilibrium and it must be a smooth, sinusoidal function of azimuth due to the interplay between the azimuthal symmetry of the COT end plates and the direction of gravity [1].

These simplifying features distinguish a drift chamber with a single active volume from the complicated geometry of a silicon tracker which is a patchwork of planar tiles.

2. Benefits of cosmic-ray alignment

The *a priori* azimuthal variation is suppressed by two orders of magnitude by the cosmic-ray alignment (see Table III). Importantly, the remaining variation is consistent with statistical scatter [1]. Further studies can therefore be performed inclusively over azimuth.

The *a priori* variability with respect to the longitudinal variables z_0 (position of the track along the z axis) and polar angle is even smaller than the azimuthal variability, reflecting a good understanding of the wire deflections due to electrostatic and gravitational forces. To achieve the ultimate goal of the accuracy of the alignment, the radial dependence of the wire shape is investigated in Ref. [21], because wire tensions likely cause the end plates to bend inward with a radius-dependent displacement. With additional tuning of the wires' shape to accommodate this hypothesis, the variability of the pulls with respect to z_0 and $\cot\theta$ is suppressed by 1–2 orders of magnitude, as shown in Ref. [21] and summarized in Table III. The pulls are largest near the edges of the phase space in z_0 and $\cot\theta$, both before and after this tuning. This is consistent with the hypothesis that inaccuracies in the wire shape are the root cause since the shape changes most rapidly at large $|z|$ [1].

The postalignment variability with respect to z_0 and $\cot\theta$ is only a factor of 1.5–2 larger than statistical scatter. Any systematic impact of averaging over this variation is further mitigated because studies with cosmic rays are performed in the same phase space as collider data: $|z_0| < 60$ cm and the fiducial acceptance of all COT superlayers. Thus, the average a_0 for cosmic-ray data matches the collider data much more closely than this residual variability.

3. Benefit of COT-beam alignment

Once the COT is internally well-aligned, accuracy of the beam coordinates is important. Upon constraining the COT track to the beam axis, a $\sin\phi$ modulation will be induced if the beam-axis coordinates are incorrect in the COT coordinate system. Equation (24) of Ref. [3] and Eq. (14) of Ref. [24] include this term in the model.

In Appendix F we show that a 1 μm misalignment of the beam axis induces a 5 PeV^{-1} bias in the beam-constrained curvature; as mentioned in Appendix B 1, the beam axis has been pinned down over the entire running period to better than this. Averaging a sinusoidal modulation over azimuth suppresses any residual bias by at least another order of magnitude. Thus, any ϕ-asymmetry due to beam-constraining will be far smaller than the 10 PeV^{-1} estimate used for Tables I and II, and subsequent studies can be performed inclusively over azimuth.

4. Ultimate Δ_{pe} tune

The a_0 parameter features prominently in the Δ_{pe} observable [Eq. (4) and Sec. IV B 1] and has been used to derive a final alignment correction as a quadratic function of $\cot\theta$, the relevant physical variable. The average over the z_0 profile of the beam luminous region applies consistently for all collider data, and azimuthal variation has already been eliminated. The azimuthal dependence modeled in Eq. (24) of Ref. [3] and Eq. (14) of Ref. [24] was not required in Eq. (S4) of Ref. [2], where no systematic azimuthal variation of Δ_{pe} was found. The parameters capturing the dependence on $\cot\theta$ have the same meaning in all three models, with a change of notation from Ref. [3] to Refs. [2,24] as mentioned in Appendix A.

The coefficient linear in $\cot\theta$ is the only one that induces a nonnegligible systematic uncertainty on m_W because it couples to the charge asymmetry in W-boson production at the Tevatron. It is strongly constrained by the cosmic-ray data which span the COT in the z direction and pin down the relative rotation between the end plates, i.e., the end-to-end twist of the COT. The twist degree of freedom for each COT supercell is explicitly measured in the cosmic-ray alignment procedure [21], which explains why the Δ_{pe} tune finds the twist coefficient to be $(0 \pm 4_{\text{stat}})\ \text{PeV}^{-1}$ (Eq. (S4) of Ref. [2]). The remaining two parabolic coefficients of the Δ_{pe} tune have nonzero values that are consistent with the imperfections in the wire-shape corrections derived from cosmic-ray data (Fig. 25 of Ref. [21]) as noted in Table III. The internal consistency of the alignment over independent control samples of data gives confidence in robustness of the procedure.

The twist coefficient induces a small systematic uncertainty of 0.8 MeV on m_W, while the remaining two parabolic coefficients have negligible impact [2].

APPENDIX E: ANALYSIS OF Δ_c^+ AND Δ_c^-

In Sec. II we used the fitted dicosmic helix' curvature c_{d} as a proxy for the true curvature c because the resolution of c_{d} is a factor of 12 better than the curvature resolution of the separate measurements of the incoming and outgoing muons. We check whether this substitution allows us to be sensitive to the systematic bias δc of Eq. (1), since the same bias may be present in c_{d}, i.e., $c_{\text{d}} = c + \delta c_{\text{d}}$. Here, δc_{d} represents the subset of terms present in δc that are capable of biasing the dicosmic fit.

In the following, we set $a_1 = 0$ without loss of generality since a_1 represents a correction to a global scale factor on curvature.

1. Analysis of Δ_c^+

The Δ_c^+ observable [Eq. (2)] is an expansion in small coefficients a_n and b_n. Consider a term in δc of the form $a_n c^n$ (where n is a positive integer) which upon substitution expands to

$$a_n c^n = a_n (c_{\text{d}} - \delta c_{\text{d}})^n \approx a_n \left(c_{\text{d}}^n - n c_{\text{d}}^{n-1} \delta c_{\text{d}}\right) = a_n c_{\text{d}}^n \left(1 - n \frac{\delta c_{\text{d}}}{c_{\text{d}}}\right)$$

to first order in δc when $n > 0$.

As $\frac{\delta c_{\text{d}}}{c_{\text{d}}} < \frac{\delta c}{c_{\text{d}}} \lesssim 10^{-4}$ (known from the measurements of Δ_{pe} and the Z boson mass [2]), the use of c_{d} as a proxy for c allows us to infer the values of the a_n coefficients with a relative accuracy better than 0.01% for $n > 0$. Replacing $a_n \to b_n q$ proves the same consequence for the b_n coefficients for $n > 0$. Thus, there is no loss of accuracy when c_{d} is substituted for c.

Since this proof fails for $n = 0$, we consider the a_0 coefficient explicitly. The use of c_{d} in Eq. (2) yields, to first order in δc as $c \to 0$,

$$\Delta_c^+ \approx a_0 + b_1 q (c_{\text{d}} - \delta c) \approx a_0 (1 - b_1 q) + b_1 q c_{\text{d}},$$

which shows that the fractional inaccuracy on the a_0 determination is given by b_1, which is negligible.

We conclude that one can use c_{d} as a proxy for c when analyzing Δ_c^+ to measure the coefficients appearing in Eq. (2) with no loss of accuracy. These conclusions have been verified by a Monte Carlo study of this observable.

2. Analysis of Δ_c^-

The use of c_{d} in Eq. (3) yields, to first order in δc as $c \to 0$,

$$\Delta_c^- \approx b_0 q + c = b_0 q + (c_{\text{d}} - \delta c_{\text{d}}).$$

Subtracting the term linear in c_{d} yields, as $c \to 0$,

$$\Delta_c^- - c_{\text{d}} = b_0 q [1 - 1 + \mathcal{O}(b_2 c)] \propto b_0 b_2 c.$$

This observable is suppressed by the b_2 factor. Furthermore, it cancels in the analysis of $|\Delta_c^- - c_{\text{d}}|$ if linear in c and is absorbed in a_1 if linear in $|c|$. We conclude that b_0 cannot be constrained by the analysis of the Δ_c^- observable.

Next, consider a term in δc of the form $b_r q |c|^r$ (where $0 < r < 1$ is a positive fraction). Without loss of generality we consider $c > 0$ since the calculation will be mirrored for $c < 0$. Therefore,

$$\Delta_c^- \approx b_r c^r + c = b_r c^r + (c_{\text{d}} - b_r c^r) \approx c_{\text{d}} \Rightarrow \Delta_c^- - c_{\text{d}} \approx 0.$$

Similarly, consider a term in δc of the form $b_2 q c^2$. For $c > 0$,

$$\Delta_c^- \approx b_2 c^2 + c = b_2 c^2 + (c_{\text{d}} - b_2 c^2) \approx c_{\text{d}} \Rightarrow \Delta_c^- - c_{\text{d}} \approx 0,$$

and the same conclusion is reached for $c < 0$ by replacing $b_2 \to -b_2$.

By extension, none of the terms in δc that show up in the Δ_c^- observable as a function of c can be extracted by studying Δ_c^- as a function of c_{d}.

The reason that the coefficients in Eq. (3) cannot be extracted by analyzing Δ_c^- versus c_{d} is that Δ_c^- represents the average of the curvature measurements of the incoming (corrected for direction of propagation) and outgoing legs of the cosmic-ray trajectory, and c_{d} represents a similar (constrained) average curvature of the entire trajectory. Thus, $\Delta_c^- \cong c_{\text{d}}$ and the analysis of Δ_c^- versus c_{d} is blind to the coefficients in Eq. (3).

APPENDIX F: SINGLE-WIRE BIAS ON CURVATURE

A curvature bias δc is related to a sagitta (d) bias as $d \sim (\delta c) l^2$ where l is the length of the track. The typical alignment accuracy of the wires is 1 μm [2,21]. For $d =$ 1 μm and $l = 1$ m, $\delta c \sim 10^{-8}\,\text{cm}^{-1} = 5\,\text{PeV}^{-1}$ for the 1.4 T

magnetic field of CDF. At $p_T \sim 40$ GeV, this curvature bias translates to a momentum bias of 200 ppm. Since a sagitta bias this large would materialize at the maximum rate of 1‰ (Sec. VI A 1), the maximum momentum calibration bias would be 200 ppm×1‰ or 0.2 ppm. Any difference of this rate between positive and negative tracks would translate to a charge-averaged mass bias; Fig. 5 suggests an additional suppression factor of 5, i.e., an upper bound on a mass bias of 40 ppb. This bound is conservative because a single-hit sagitta does not translate into a track sagitta given the large number of hits.

A similar calculation based on the superlayer efficiency variation of (at most) 0.1‰ (Sec. VI A 1) provides an even more stringent (and more realistic) bound of 4 ppb on a mass bias due to possible curvature-dependent pattern-recognition effects in the $c \to 0^{\pm}$ limit.

APPENDIX G: A MODEL FOR $b_0 q$ TERM IN CURVATURE RESPONSE

The difficulty of creating a COT model that will generate a $b_0 q$ term in the curvature response is that as $c \to 0$ there is no information available to the COT on which a charge-dependent effect can be based. This observation leads to the conclusion that, in this limit, the particle's charge can only be known to the particle itself. Therefore, such a discontinuous response can only be generated by the particle's local interactions and not by the COT.

An example of a particle-interaction model is an energy loss that grows quadratically with energy, $p_T^{\rm loss} = b_0 p_T^2$. Therefore,

$$\delta c = \frac{q}{p_T - b_0 p_T^2} - \frac{q}{p_T} = \frac{q}{p_T}\left(\frac{1}{1 - b_0 p_T} - 1\right) = \frac{q}{p_T}\frac{b_0 p_T}{1 - b_0 p_T} \approx b_0 q,$$

where energy conservation requires the fractional energy loss to be within the range $0 \leqslant b_0 p_T < 1$. In practice, the consistency of the m_Z measurement using the J/ψ and Υ-based calibrations [2] implies that $b_0 p_T < 100$ ppm as shown in Sec. VI B 3. Thus, the $b_0 p_T$ term can be neglected in the denominator and this energy-loss model induces the $b_0 q$ term with $b_0 > 0$.

The reasoning is that, since the p_T always reduces independent of charge, the change in curvature has the same sign as the charge, even as $c \to 0$, because the particle's charge is conserved. We also note that this model cannot generate $b_0 < 0$ because it is impossible to mimic a particle gaining energy during propagation.

Synchrotron radiation off a charged particle in a magnetic field causes an energy loss per revolution that is proportional to γ^4/R, where $\gamma = E/m$ is the energy to mass ratio, i.e., the Lorentz boost factor, and R is the radius of the particle's circular arc [25]. As $R \propto E$ for a fixed magnetic field and polar angle, the reduction in the track p_T is $p_T^{\rm loss} \propto E^3$ per revolution. The fraction of a revolution executed inside the COT is $l/(2\pi R)$ where l is the radius of the COT. Scaling $p_T^{\rm loss}$ by this fraction yields the result $p_T^{\rm loss} \propto E^3/R \propto E^2 \propto p_T^2$, or $p_T^{\rm loss} = b_0 p_T^2$. For a muon of $p_T = 40$ GeV, $p_T^{\rm loss}$ evaluates to 3 meV (millielectron Volt) [25], corresponding to a vanishingly small $b_0 p_T = 0.0001$ ppb.

If we imagine an energy loss model of the form $p_T^{\rm loss} = b_r p_T^{2-r} = -\delta p_T$, then it leads to

$$b_r p_T^{-r} = -\frac{\delta p_T}{p_T^2} = q\delta c = b_r |c|^r \Rightarrow \delta c = q b_r |c|^r.$$

As shown in Sec. VI B 3, positive values of b_0 or b_r bias the measured mass to lower values, as expected from an unanticipated process of energy loss from the leptons.

[1] T. Affolder *et al.*, CDF Central Outer Tracker, Nucl. Instrum. Methods Phys. Res. Sect. A **526**, 249 (2004).

[2] T. Aaltonen *et al.* (CDF Collaboration), High-precision measurement of the *W* boson mass with the CDF II detector, Science **376**, 170 (2022).

[3] T. Aaltonen *et al.* (CDF Collaboration), First run II measurement of the *W* boson mass at the Fermilab Tevatron, Phys. Rev. D **77**, 112001 (2008).

[4] K. R. Popper, *Objective Knowledge: An Evolutionary Approach* (Oxford University Press, Oxford, UK, 1972).

[5] J. L. Amey, J. Keeley, T. Choudhury, and I. Kuprov, Neural network interpretation using descrambler groups, Proc. Natl. Acad. Sci. USA **118**, e2016917118 (2021).

[6] G. Charpak, R. Bouclier, T. Bressani, J. Favier, and C. Zupancic, The use of multiwire proportional counters to select and localize charged particles, Nucl. Instrum. Methods **62**, 262 (1968).

[7] M. R. Adams *et al.* (E665 Collaboration), Proton and deuteron structure functions in muon scattering at 470 GeV, Phys. Rev. D **54**, 3006 (1996).

[8] A. V. Kotwal, Proton and deuteron structure functions in muon scattering at 470 GeV, Ph.D. thesis, Harvard University, 1995.

[9] G. Aad *et al.* (ATLAS Collaboration), Observation of a new particle in the search for the Standard Model Higgs boson with the ATLAS detector at the LHC, Phys. Lett. B **716**, 1 (2012).

[10] S. Chatrchyan *et al.* (CMS Collaboration), Observation of a new boson at a mass of 125 GeV with the CMS experiment at the LHC, Phys. Lett. B **716**, 30 (2012).

[11] R. Aaij *et al.* (LHCb Collaboration), Measurement of the *W* boson mass, J. High Energ. Phys. 01 (2022) 036.

[12] A. Aryshev *et al.* (ILC International Development Team Collaboration), The international linear collider: Report to Snowmass 2021, arXiv:2203.07622.

[13] H. Cheng *et al.* (CEPC Physics Study Group), The physics potential of the CEPC. Prepared for the US snowmass community planning exercise (Snowmass 2021), arXiv:2205.08553.

[14] J. de Blas *et al.* (CLIC Collaboration), The CLIC potential for new physics, arXiv:1812.02093.

[15] A. Blondel and P. Janot, FCC-ee overview: New opportunities create new challenges, Eur. Phys. J. Plus **137**, 92 (2022).

[16] P. Azzurri, The W mass and width measurement challenge at FCC-ee, Eur. Phys. J. Plus **136**, 1203 (2021).

[17] J. Benesch *et al.* (MOLLER Collaboration), The MOLLER experiment: An ultra-precise measurement of the weak mixing angle using Møller scattering, arXiv:1411.4088.

[18] J. Arrington *et al.* (Jefferson Lab SoLID Collaboration), The solenoidal large intensity device (SoLID) for JLab 12 GeV, arXiv:2209.13357.

[19] D. Becker *et al.*, The P2 experiment, Eur. Phys. J. A **54**, 208 (2018).

[20] H. Akaike, A new look at the statistical model identification, IEEE Trans. Auto. Control **19**, 716 (1974).

[21] A. V. Kotwal and C. Hays, Drift chamber alignment using cosmic rays, Nucl. Instrum. Methods Phys. Res. Sect. A **762**, 85 (2014).

[22] A. Sill *et al.*, CDF Run II silicon tracking projects, Nucl. Instrum. Methods Phys. Res. Sect. A **447**, 1 (2000).

[23] A. V. Kotwal, H. K. Gerberich, and C. Hays, Identification of cosmic rays using drift chamber hit timing, Nucl. Instrum. Methods Phys. Res. Sect. A **506**, 110 (2003).

[24] T. Aaltonen *et al.* (CDF Collaboration), Precise measurement of the W-boson mass with the Collider Detector at Fermilab, Phys. Rev. D **89**, 072003 (2014).

[25] J. D. Jackson, *Classical Electrodynamics*, 2nd ed. (Wiley, New York, NY, 1975).